Geochemistry and Petrogenesis of Late Ediacaran Rare-metal Albite Granites of the Arabian-Nubian Shield

Bassam A. ABU AMARAH[1*], Mokhles K. AZER[2], Paul D. ASIMOW[3], Habes GHREFAT[1] and Heba S. MUBARAK[2,*]

[1]*Department of Geology and Geophysics, King Saud University, Riyadh 11451, Saudi Arabia*
[2]*Geological Sciences Department, National Research Centre, Cairo, Egypt*
[3]*Division of Geological & Planetary Sciences, California Institute of Technology, Pasadena CA 91125 USA*

Abstract: The Abu Dabbab albite granite (ADAG), in the central Eastern Desert of Egypt, hosts the most significant rare metal ore deposit in the northern part of the Neoproterozoic Arabian-Nubian Shield. Here, we report detailed field, petrographic, mineralogical and geochemical investigation of the ADAG, an isolated stock-like granitic body with sharp intrusive contacts against metamorphic country rocks, probably emplaced at about 600 Ma. The fine-grained porphyritic upper unit is a preserved remnant of the shallowly-emplaced apex of the magma chamber, whereas the medium-grained lower unit crystallized at deeper levels under subvolcanic conditions. The peraluminous leucocratic ADAG shares common geochemical characteristics with post-collisional intraplate A-type magmas. In addition to the conspicuous enrichment in Na_2O, the ADAG is remarkable for its anomalous concentrations of Ta, Nb, Li, Hf, Ga, Sn, Zn and heavy rare-earth elements. Nb-Ta minerals in the ADAG are mixed with Fe-Mn oxides, forming black patches that increase in abundance toward of the base of the intrusion. Columbite–tantalite, cassiterite and wolframite are the most important ore minerals. Pronounced negative Eu anomalies (Eu/Eu* = 0.10-0.24) reflect extreme magmatic fractionation and perhaps the effects of late fluid-rock interaction. The ADAG was most likely generated by partial melting of the juvenile middle crust of the ANS as the geotherm was elevated by erosional uplift following lithospheric delamination and it was emplaced at the intersection of lineations of structural weakness. Although formation of the ADAG and its primary enrichment in rare metals are essentially due to magmatic processes, late-stage metasomatism caused limited redistribution of rare metals. Fluid-driven subsolidus modification was limited to the apex of the magma chamber and drove development of greisen, amazonite, and quartz veins along fracture systems.

Key words: Arabian-Nubian Shield, post-collisional, rare-metal bearing granite, stockscheider pegmatite, greisen, amazonite, tetrad effect

1 Introduction

The Arabian–Nubian Shield (ANS) exposes crystalline rocks of Neoproterozoic age and represents one of the largest tracts of juvenile crust on Earth (Meert, 2003; Johnson, 2003; Stoeser and Frost, 2006; Ali et al., 2010; Khalil et al., 2014, Samuel et al., 2019). It constitutes the northern part of the East African Orogen (Stern, 1994) and is well-exposed in parts of Egypt, Saudi Arabia, Sudan, Eritrea, Ethiopia, Yemen and Somalia (Fig. 1). It was formed through accretion of oceanic island arc terranes and associated ophiolite remnants that amalgamated during the collision of East and West Gondwana upon closure of the Mozambique Ocean (e.g. Meert, 2003; Ali et al., 2010; Johnson et al., 2013). Late Neoproterozoic rock outcrops in the Eastern Desert of Egypt form the extreme northern end of the Nubian Shield, which was contiguous with the Arabian Shield before the opening of the Red Sea.

* **Corresponding author:** Dr. Bassam A. Abu Amarah (babuamarah@ksu.edu.sa)

This article has been accepted for publication and undergone full peer review but has not been through the copyediting, typesetting, pagination and proofreading process, which may lead to differences between this version and the Version of Record. Please cite this article as doi: 10.1111/1755-6724.14379.

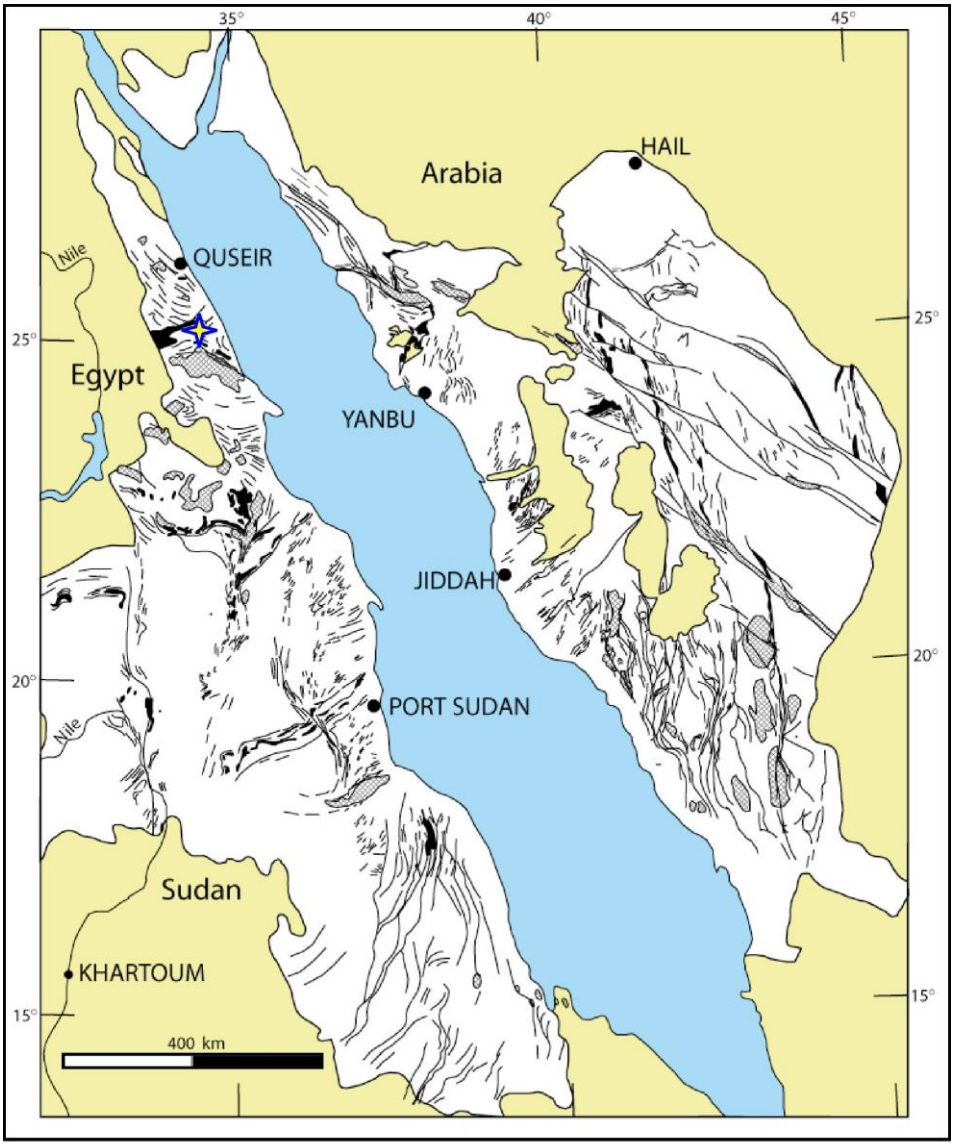

Fig. 1. Simplified map of the Arabian-Nubian shield (After Johnson and Woldehaimanot, 2003). Basement outcrops are white; Phanerozoic cover is shown in yellow; structural trends are highlighted; ophiolitic rocks are shown in black and gneissic rocks shown in stipple. The location of the Abu Dabbab area is indicated by a yellow star.

The ANS has been intruded by voluminous granitoids of various ages, geochemical characteristics and tectonic regimes (e.g. Qadhi, 2007; Küster, 2009; Ali et al., 2014; Moghazi et al., 2015; Khalil et al., 2018; Basta et al., 2017; Abdallah et al., 2019). One of the most striking features of the north ANS is the abundance of post-collisional granitic intrusions. Some of these granitic plutons are enriched in rare metals and often modified by metasomatic processes including albitization and greisenization. The style of mineralization of these granites differs from one pluton to another (e.g. Helba et al., 1997; Moghazi et al., 2015; El Hadek et al., 2016; Abu El-Rus et al., 2017). The rare-metal granites of the ANS have received much attention due to their substantial economic significance as sources of Nb, Ta, rare-earth elements (REE), U, Zr and Th (e.g. Qadhi, 2007; Ali et al., 2014; Moghazi et al., 2015). Despite numerous studies and widespread outcrops in the ANS, however, there remains considerable controversy about their origin and geotectonic evolution.

In this context, the Abu Dabbab albite granite (ADAG) in the central Eastern Desert provides a good opportunity to understand the petrogenetic processes leading to the formation of mineralized post-collisional granites. The ADAG is one of the largest granite-hosted rare metal (Ta-Sn-Nb) deposits in the Eastern Desert (Sabet et al., 1976). This contribution aims to integrate field observations, petrography, mineral chemistry and whole-rock chemical analyses to discern the petrological characteristics, magmatic evolution, mineralization processes, and geodynamic setting of the Abu Dabbab intrusion.

2 Geologic setting

The study area around Gabal Abu Dabbab is located about 50 km NW of Marsa Alam town along the Red Sea (Fig. 2a), at 25° 20\ 40\\ N and 34° 32\ 35\\ E. The ~1 km^2 study area mapped in Fig. 2b is covered mainly by metamorphic rocks, including serpentinite, talc-carbonate rocks, metavolcanic units and metasedimentary outcrops. The regional metamorphic rocks were deformed and equilibrated under greenschist facies conditions (Renno, 1997). Faults and shear zones affecting the study area are mostly grouped into two roughly perpendicular sets trending NW-SE and NE-SW. A few N-S trending basalt and aplite dykes cut through the metamorphic country rocks and are truncated by the ADAG. The northeastern margin of the Abu Dabbab granitic mass is bounded by major NW-SE sinistral strike-slip shear zones that belong to the Najd Fault System (Stern, 1985), whereas the other margins are unfaulted intrusive contacts that preserve sheared albite granite presumably associated with the original emplacement of the pluton. The field relations indicate that the ADAG predated or possibly was coeval with motion on the Najd fault system, which has been dated at ~600 Ma (Stern, 1985; Boskabadi et al., 2017). Carbonation of the ophiolitic country rocks along the Najd system was probably related to Najd deformation and is also ~600 Ma old. Direct age determination of the ADAG remains imprecise (Renno, 1997), but the emplacement of the intrusion can be bracketed between 585 and 610 Ma, and is thus related to the post-tectonic magmatic period of the ANS.

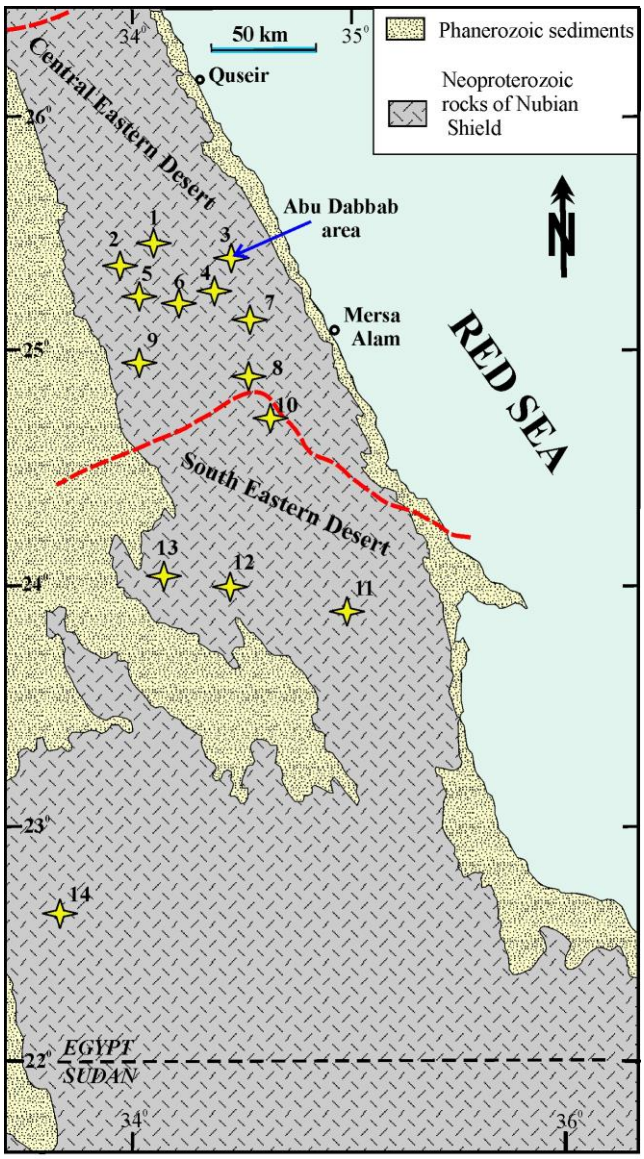

Figure 2a

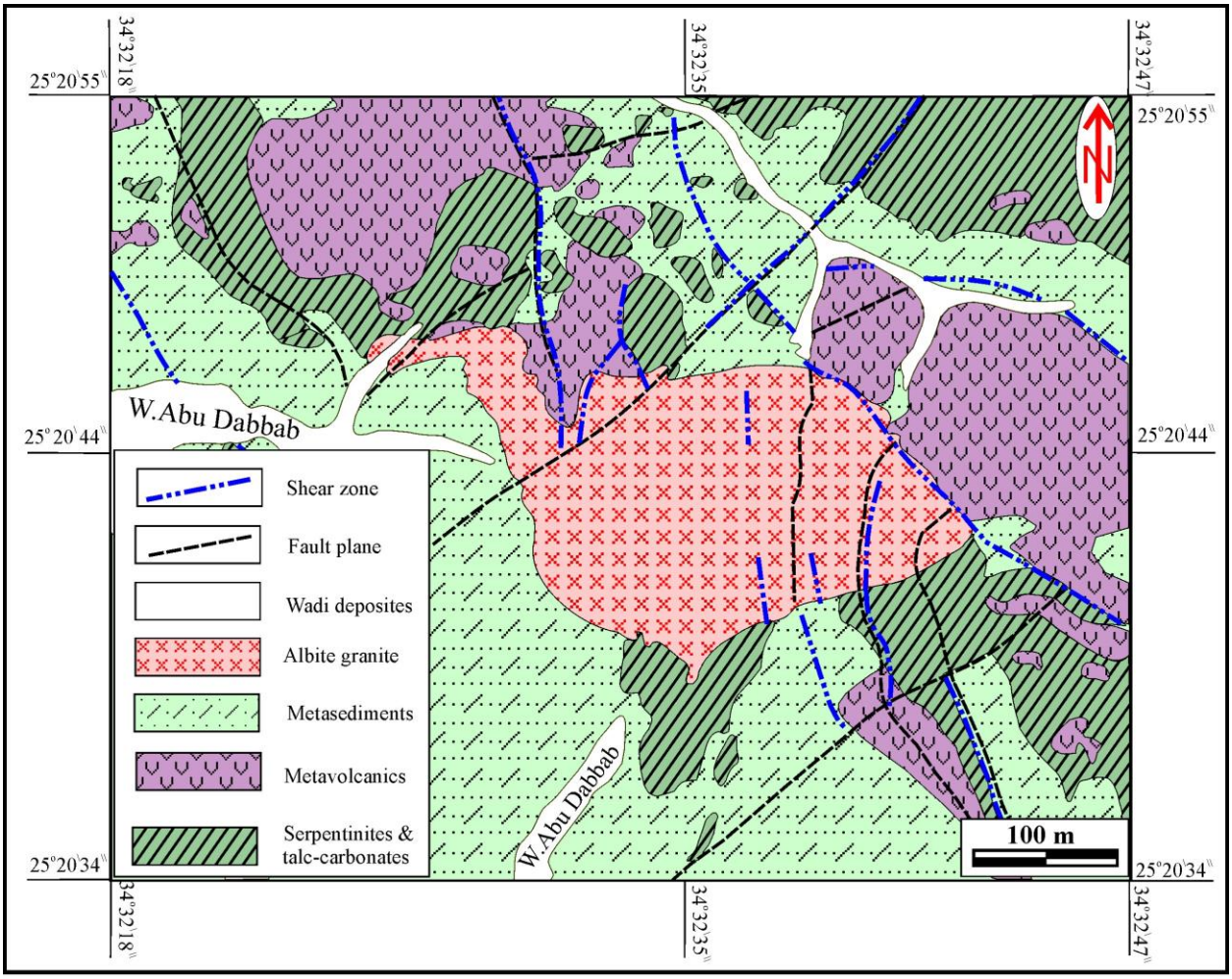

Figure 2b

Fig. 2. Maps of rare-metal granites in Egypt.
(a) Distribution of the most important rare-metal bearing granite intrusions in the central and south Eastern Desert of Egypt: (1) Umm Naggat, (2) Umm Samra, (3) Abu Dabbab, (4) Nuweibi, (5) Ineiga, (6) Homrit Waggat, (7) Igla, (8) Zabara, (9) Muweilha, (10) Nugrus, (11) El-Gharabiya, (12) Nikeiba, (13) Homrit Akarem, (14) Um Hibal, and (15) Um Ara. The dividing line between central and southern portions of the Nubian Shield is after Stern and Hedge (1985). (b) Geological map of the Abu Dabbab area (modified after Heikal et al., 2018).

The ADAG forms an ellipsoidal intrusive stock, elongated in an E–W direction. A large off-shoot of the intrusion extends ~150 m from the northwestern margin of the ADAG body. Contacts between the ADAG and its metamorphic country rocks are knife-sharp. The metavolcanic and metasedimentary units nearest the intrusion were modified by contact metamorphism to amphibolite and hornfels. The albite granite is generally massive, but deformation extending up to cataclasis is apparent in major shear zones along the periphery of the pluton.

The ADAG is a fine- to medium-grained, holocrystalline, leucocratic granite. It is devoid of xenoliths, enclaves, or dykes. Near the southern margin of the intrusion, it is partly porphyritic in texture. Contacts between the porphyritic and non-porphyritic types are irregular and gradational, indicating contemporaneous emplacement. The albite granite

exhibits chilled margins (10 to 25 cm wide) near the contact with the ophiolitic metavolcanic country rocks. A weak magmatic foliation was noted in the field at selected outcrops, but it was only visible if the outcrops were observed while wet from recent rains. In the southern, porphyritic portion of the intrusion, there are a few outcrops of breccia with angular clasts suggesting explosive, in-situ formation; the breccia is not related to shear zones.

Locally, there are a variety of mineralized zones both along the margins and in the interior of the pluton. The interior is sometimes enriched in rounded or dendritic dark-colored patches (Fig. 3a). The black patches are variable in size (0.5-2.0 cm) and abundance; they are generally concentrated toward the northern margin of the intrusion. The southern margin features veins from 50 to 400 m long and from 10 to 50 cm wide, consisting of stockscheider pegmatite, quartz, greisen or albitite. The veins generally strike N–S and NE–SW and locally extend up to 200 m into the country rocks. There is stockscheider pegmatite associated with nests of fluorite crystals in cross-cutting veins at the southwestern contact of the intrusion (Fig. 3b, c). Greisen occurs as thin veins (5-40 cm), especially along the southeastern margin, sometimes extending into the country rocks. Greisen (Fig. 3d) and albitite (Fig. 3e) also form 5-10 cm wide selvages bounding quartz veins at the margins of the intrusion.

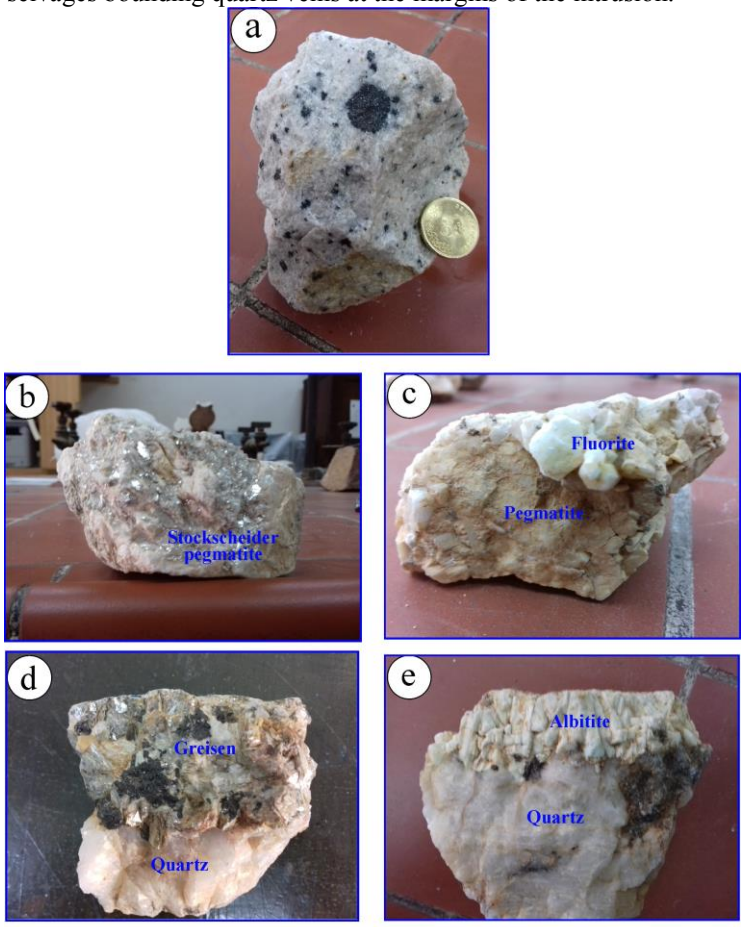

Figure 3

Fig. 3. Hand specimen photographs of the studied rocks. (a) dark-colored patches of manganese–iron oxide hosting Nb-Ta minerals in the medium-grained albite granite, (b) stockscheider pegmatite, (c) nests of fluorite crystals associate with pegmatite, (d) selvage of greisen bounding a quartz vein, and (e) selvage of albitite associated with a quartz vein.

3 Petrography

Based on the petrographic studies and textural variations, samples of the Abu Dabbab intrusion can be divided into albite granite, cataclastic albite granite, albitized granite (albitite), and greisen. The main albite granite is further divided into two units with the same mineralogical composition: a medium-grained albite granite and a fine-grained porphyritic variety. Petrographic study documents several types of alteration including greisenization, amazonite replacement, albitization, and impregnation with secondary Mn-minerals. In this section we describe the detailed petrographic characteristics of each primary and altered rock type.

Medium-grained leucocratic albite granite is the most common rock type in the Abu Dabbab intrusion. It consists mainly of albite, quartz, and alkali feldspars with minor interstitial muscovite. Accessory minerals include cassiterite, columbite–tantalite, Fe-Ti oxides, zinnwaldite, allanite, zircon, fluorite, titanite, apatite, garnet and topaz. *Albite* is the most abundant mineral, occurring as subhedral to euhedral crystals up to 1.5 mm long or as small interstitial laths. Albite also occurs as small euhedral laths (≤0.15 mm long) included in quartz and K-feldspars. *Quartz* occurs either as subhedral to anhedral large crystals (up to 2.5 mm across) or as fine (≤0.5 mm), anhedral interstitial grains. The large quartz crystals contain small inclusions of albite, muscovite and topaz (Fig. 4a); in a few cases albite laths included in quartz are arranged concentrically along growth zones, giving rise to snowball texture (Fig. 4b). *K-feldspars*, both orthoclase and microcline, occur as euhedral to anhedral crystals (up to 3 mm across). Some are perthitic, with both patch and vein types. Some K-feldspars are partially replaced by albite and/or muscovite. Microcline is not abundant; it occurs as anhedral crystals up to 1.0 mm across filling interstices between the quartz and albite. It is partly or completely replaced by albite (Fig. 4c). Amazonite is observed in a few samples near the margins of the intrusion, as anhedral aggregates (Fig. 4d) or as veinlets (Fig. 4e). Primary *muscovite* is colorless to pale green and occurs as subhedral to euhedral crystals corroded by secondary albite and quartz (Fig. 4f) or as inclusions in large quartz crystals. Secondary muscovite forms anhedral crystals with albite lath inclusions (Fig. 4g). Rare relics of *biotite* are observed in a few muscovite crystals.

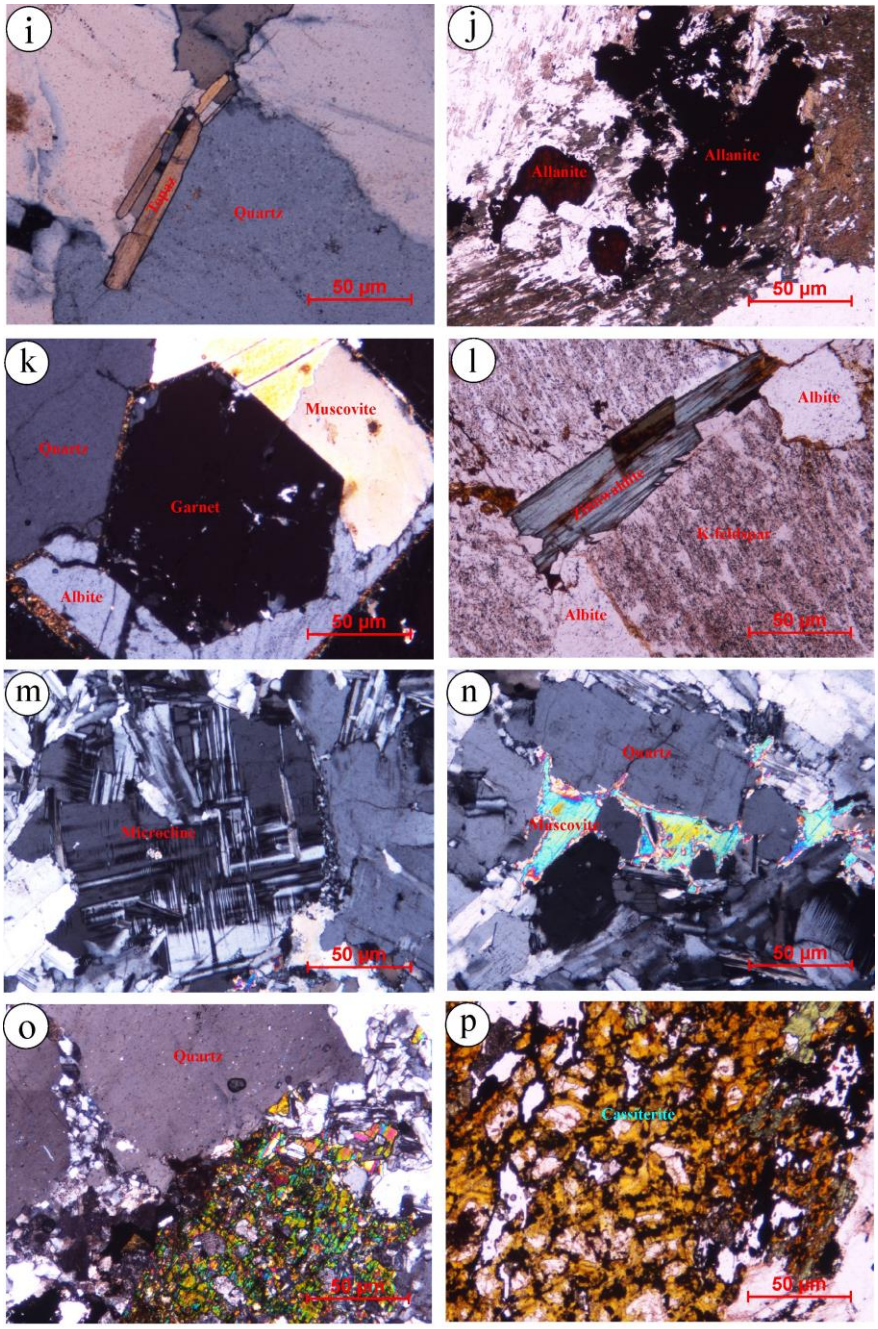

Figure 4 cont.

Fig. 4. Selected photomicrographs from the Abu Dabbab albite granite.

Images d, e, j, l and p are taken under plane-polarized light, while the other images are taken under crossed Nicols: (a) small inclusions of muscovite and albite in large quartz crystal, (b) snowball texture with concentrically arranged albite laths along the growth surface of quartz, (c) microcline partly replaced by albite, (d) anherdal aggregations of amazonite, (e) amazonite filling veinlets, (f) primary muscovite corroded by secondary albite and quartz, (g) secondary muscovite including anhedral albite laths, (h) dispersed crystals of bladed columbite, (i) Tabular crystal of topaz, (j) anhedral crystals of allanite, (k) euhedral crystal of garnet showing hexagonal cross-section, (l) pale brown tabular crystal of zinnwaldite, (m) microcline

phenocryst partly replaced by albite, (n) muscovite replacing feldspars, (o) protomylonite texture featuring large crystals of quartz surrounded by broken crystals of quartz and albite with abundance of secondary minerals, and (p) cassiterite filling the fractures in the cataclastic albite granite.

The albite granite includes a remarkable variety of accessory minerals. *Columbite–tantalite* occurs as bladed or prismatic euhedral to subhedral dispersed crystals (Fig. 4h) and as inclusions in the quartz phenocrysts. *Cassiterite* occurs as disseminated crystals (up to 0.3 mm long), sometimes associated with mica and topaz. *Topaz* forms euhedral to subhedral inclusions in quartz and interstitial anhedral crystals (Fig. 4i). Near contacts with the country rocks and greisen veins, topaz coexists with *beryl* and muscovite. *Fluorite* occurs as small (<2 mm) anhedral interstitial crystals among the feldspars or, rarely, as veins along through-going fractures that suggest a deuteric origin (Tollo et al., 2004). *Allanite* is common as strongly pleochroic reddish-brown anhedral crystals (Fig. 4j). *Garnet* occurs mainly as euhedral crystals (0.1-0.2 mm) with hexagonal cross-sections and sparse inclusions (Fig. 4k). *Zinnwaldite* (i.e., siderophyllite-polylithionite series) occurs as pale brown tabular crystals (Fig. 4i).

Porphyritic albite granite is restricted to the southern portion of the Abu Dabbab granitic mass; it has the same mineralogical composition as the dominant medium-grained albite granite. It consists of euhedral to subhedral phenocrysts of albite, quartz, K-feldspar and microcline embedded in a fine groundmass of feldspars and quartz (Fig. 4m). Two generations of albite are recognized: an early phase represented by large turbid phenocrysts and a later phase of clear small laths in the groundmass or replacing K-feldspars. Rarely, the quartz phenocrysts feature snowball texture defined by albite lath inclusions oriented along growth surfaces. Muscovite occurs as irregularly distributed flakes in the groundmass or replacing feldspars (implying subsolidus metasomatism) (Fig. 4n). The most abundant accessory minerals are Fe-Ti oxides, cassiterite, columbite–tantalite, topaz, and fluorite. Garnet and zircon are present but rare.

The cataclastic variety of albite granite has the same mineralogical composition as the main phases except for enrichment in secondary muscovite. It is affected by various degrees of alteration and brittle deformation, shown by ground, fractured and broken crystals (Fig. 4o). The texture varies from protomylonite, with large surviving porphyritic crystals of quartz and feldspars, to typical mylonitic granite with a foliated matrix. Most fractures are filled with secondary minerals including quartz, cassiterite, *chlorite* and *sericite* (Fig. 4p). Many large fractured feldspar crystals are intensely replaced by quartz, suggesting that Si enrichment continued after complete consolidation of the albite granite. Cassiterite is concentrated along the fractures as anhedral aggregates.

Albitite veinlets are dominantly fine-grained and composed mainly of albite (65–80 %), quartz (10-15%), and K-feldspar (3-5 %) with accessory muscovite, *iron oxides*, fluorite and *calcite*. The subhedral and anhedral albite prisms show resorbed and diffuse grain boundaries. The rare relics of microcline and orthoclase are included in albite. Quartz occurs as anhedral to serrated irregular crystals. Anhedral flakes of muscovite and fluorite are interstitial to albite and quartz.

Greisen is a light-colored rock consisting essentially of aggregates of quartz grains and anhedral mica flakes with highly corroded albite and K-feldspar relics. Accessory minerals include cassiterite, *wolframite*, fluorite, topaz, *tourmaline* and beryl. Quartz forms large anhedral crystals (1-4 mm) embedded in subhedral aggregates of quartz and mica. Topaz forms excellent stubby idiomorphic crystals. Fluorite occurs as small anhedral crystals.

Quartz veins consist essentially of quartz with accessory mica, topaz, cassiterite, beryl, fluorite, wolframite and native *copper*. Euhedral bipyramidal to subhedral cassiterite crystals may be quite coarse, up to 1 cm. It is characterized by oscillatory zoning with successively alternating zones of white, pale orange, and deep orange extending parallel to the c-axis. Beryl is concentrated towards contacts between quartz veins and their host rocks. It is present as greenish yellow and pale brown hexagonal prisms up to 0.5 mm in size, associated with topaz, muscovite and fluorite.

4 Mineral chemistry

The principal rock-forming minerals (albite, K-feldspars, and muscovite) in the ADAG samples were analyzed by electron microprobe to support petrographic mineral identification. Although numerous accessory minerals were noted in thin section, most of them could not be sensibly analyzed by electron probe with the analytical protocol used; only garnet was analyzed. The chemical formulas of the analyzed minerals were recalculated manually or with the Minpet software program of Richard (1995).

Representative analyses of albite are given in Table 1. Albite has low K_2O (<0.2 wt.%) and CaO (0.1-0.5 wt.%.) contents. The early large albite crystals have higher Ab contents (98-99%) than the later albite (96-97%).

Perthitic and non-perthitic K-feldspar analyses are given in Table 2. The non-perthitic K-feldspars are homogenous, nearly pure orthoclase (Or = 98-99%). The perthitic orthoclase and microcline have lower Or contents (93-97%). We have not attempted to reconstruct pre-exsolution bulk compositions of the perthite.

Table 1. Representative microprobe analyses of albite in Abu Dabbab albite granite.

Rock type	AD28										AD36							
Spot No.	#1	#2*	#3	#4*	#5	#6	#7*	#8	#9	#10*	#1	#2*	#3	#4	#5*	#6	#7*	#8
Major oxides (wt.%)																		
SiO_2	68.601	67.764	68.974	67.891	69.356	68.556	68.151	68.992	69.279	68.688	68.414	68.743	68.853	68.972	67.707	69.291	68.898	69.337
TiO_2	0.003	0.009	0.002	0.004	0.035	0.005	0	0.016	0.001	0.007	0.005	0.013	0.024	0.005	0.003	0.017	0.007	0.005
Al_2O3	20.506	20.185	20.343	20.426	20.101	20.182	20.116	20.385	20.138	20.67	19.413	19.828	20.785	19.776	20.295	19.39	20.271	18.884
FeO	0.004	0.128	0.017	0.058	0.02	0.056	0	0.078	0.079	0.05	0.231	0.141	0.018	0.233	0.099	0.465	0.116	0.462
MnO	0.002	0.009	0.004	0	0.006	0	0	0.005	0.004	0	0.006	0	0	0.012	0.004	0.003	0.001	0.002
MgO	0	0	0	0.001	0	0	0	0	0	0	0	0	0	0	0	0	0	0
CaO	0.199	0.433	0.167	0.541	0.155	0.138	0.478	0.16	0.073	0.367	0.081	0.316	0.261	0.152	0.454	0.123	0.439	0.112
Na_2O	11.495	11.353	11.493	11.287	11.617	11.495	11.283	11.193	11.598	11.316	11.67	11.401	11.412	11.609	11.243	11.507	11.338	11.495
K_2O	0.06	0.054	0.058	0.09	0.065	0.061	0.084	0.07	0.064	0.062	0.067	0.131	0.056	0.117	0.064	0.077	0.068	0.082
Total	100.87	99.935	101.058	100.298	101.355	100.493	100.112	100.899	101.236	101.16	99.887	100.573	101.409	100.876	99.869	100.873	101.138	100.379
	Structural formula based on 8 oxygens																	
Si	2.720372757	2.71232301	2.730075798	2.707571437	2.737151596	2.72878708	2.722990251	2.735091527	2.737326643	2.716014235	2.739655811	2.734053871	2.715853622	2.734922083	2.711832501	2.747652989	2.724910518	2.763008199
Al	1.084220614	1.077233535	1.073601298	1.08614994	1.057721211	1.071092846	1.071653082	1.077513157	1.060913772	1.089758798	1.03653128	1.051468419	1.093131116	1.045560887	1.083819804	1.025183482	1.068955289	1.003343993
Ti	0.000118965	0.000360234	7.91625E-05	0.000159525	0.001381284	0.000199019	0	0.000634298	3.95116E-05	0.000276789	0.000200226	0.000517037	0.000946662	0.000198263	0.000120157	0.000674115	0.000276849	0.000199245
Fe	0.00031724	0.01024666	0.001345762	0.004626214	0.00157861	0.004458022	0	0.006184402	0.006242839	0.003954132	0.018500906	0.011215734	0.001419992	0.018478132	0.007930389	0.036878055	0.009175582	0.03682045
Mn	0.00015862	0.000720468	0.00031665	0	0.000473583	0	0	0.000396436	0.000316093	0	0.000480543	0	0	0.000951663	0.00032042	0.000237923	7.90998E-05	0.000159396

Mg	0	0	0	7.97623E-05	0	0	0	0	0	0	0	0	0	0	0	0	0	0
Ca	0.015782691	0.034662531	0.013220131	0.043151409	0.012234226	0.01098584	0.038197219	0.012685953	0.005768699	0.029023329	0.006487331	0.025135971	0.020589888	0.012054403	0.036367642	0.00975484	0.034724831	0.00892617
Na	1.823336968	1.81766148	1.819628332	1.800554348	1.833871047	1.830177226	1.803260348	1.774923438	1.833023826	1.789798339	1.869312323	1.813767114	1.800550247	1.841310123	1.801239624	1.825186125	1.793668058	1.832255751
K	0.0095172	0.00864562	0.009182845	0.014357215	0.010260964	0.009712119	0.013424964	0.011100209	0.010114979	0.009806248	0.010732127	0.020840583	0.008835508	0.018557437	0.010253432	0.012213377	0.010757579	0.013070463
End members (wt.%)																		
Or	0.51	0.46	0.50	0.77	0.55	0.52	0.72	0.62	0.55	0.54	0.57	1.12	0.48	0.99	0.55	0.66	0.58	0.70
Ab	98.63	97.67	98.78	96.90	98.79	98.88	97.22	98.68	99.14	97.88	99.09	97.53	98.39	98.36	97.48	98.81	97.53	98.81
An	0.85	1.86	0.72	2.32	0.66	0.59	2.06	0.71	0.31	1.59	0.34	1.35	1.13	0.64	1.97	0.53	1.89	0.48

* later albite

Large sparse crystals of muscovite and fine flakes replacing feldspars were each analyzed (Table 3). The large, sparse muscovite crystals are considerably higher in TiO_2, Al_2O_3, and Na_2O but lower in MgO and SiO_2 than the fine flakes. This chemical difference supports the textural assignment of the large sparse crystals as primary and the fine flakes as secondary (Fig. 5) (Miller et al., 1981).

Table 3. Electron microprobe analyses of muscovites in the albite granite of Abu Dabbab.

Sample No	AD28									AD36								
Mineral	Primary muscovite						Secondary muscovite			Primary						Secondary		
Spot No.	#1	#2	#3	#4	#6	#7	#1	#2	#3	#1	#2	#3	#4	#5	#6	#1	#2	#3
Major oxides (wt.%)																		
SiO_2	46.077	46.795	46.702	46.807	46.404	46.756	45.435	45.998	46.021	46.765	46.164	45.122	45.743	46.112	45.312	45.336	45.869	45.156
TiO_2	0.088	0.069	0.097	0.106	0.067	0.073	0.346	0.369	0.386	0.075	0.112	0.102	0.068	0.089	0.112	0.451	0.077	0.422
Al_2O_3	27.452	29.347	29.834	30.368	29.398	29.105	26.715	25.546	25.846	29.308	28.545	28.644	30.31	29.794	28.194	25.886	28.648	27.81
FeO	5.199	4.908	5.659	1.786	4.451	4.847	5.45	5.646	5.895	4.053	5.249	7.209	2.198	6.149	7.259	6.526	4.494	5.373
MnO	1.157	1.139	0.037	0.635	1.265	1.179	0.594	0.544	0.544	1.171	1.533	0.015	0.87	0.046	0.027	0.737	1.252	0.77
MgO	0.332	0.354	0.396	0.236	0.443	0.494	2.261	2.747	2.0942	0.484	0.535	0.326	0.281	0.336	0.336	1.574	0.468	2.776
CaO	0.042	0.035	0.024	0.01	0.032	0.037	0.032	0.016	0.054	0.035	0.031	0.007	0.024	0.067	0.109	0.13	0.036	0.046
Na2O	0.227	0.245	0.193	0.308	0.266	0.306	0.195	0.143	0.0281	0.271	0.289	0.213	0.262	0.243	0.171	0.134	0.255	0.14
K2O	10.598	10.546	10.894	10.595	10.352	10.43	10.641	10.467	10.678	10.589	10.475	10.584	10.745	10.384	9.204	9.354	10.531	10.266
Total	91.172	93.438	93.836	90.851	92.678	93.227	91.669	91.476	91.5463	92.751	92.933	92.222	90.501	93.22	90.724	90.128	91.63	92.759
Structural formula based on 24 oxygens																		
Si	6.596	6.508	6.469	6.562	6.492	6.516	6.488	6.578	6.586	6.527	6.491	6.423	6.48	6.435	6.499	6.571	6.509	6.362
A^{IIV}	1.404	1.492	1.531	1.438	1.508	1.484	1.512	1.422	1.414	1.473	1.509	1.577	1.52	1.565	1.501	1.429	1.491	1.638
Al^{VI}	3.224	3.315	3.336	3.576	3.336	3.293	2.98	2.88	2.942	3.344	3.218	3.225	3.536	3.331	3.261	2.989	3.297	2.977
Ti	0.009	0.007	0.01	0.011	0.007	0.008	0.037	0.04	0.042	0.008	0.012	0.011	0.007	0.009	0.012	0.049	0.008	0.045

Fe^{2+}	0.622	0.571	0.656	0.209	0.521	0.565	0.651	0.675	0.706	0.473	0.617	0.858	0.26	0.718	0.871	0.791	0.533	0.633
Mn	0.14	0.134	0.004	0.075	0.15	0.139	0.072	0.066	0.066	0.138	0.183	0.002	0.104	0.005	0.003	0.09	0.15	0.092
Mg	0.071	0.073	0.082	0.049	0.092	0.103	0.481	0.586	0.447	0.101	0.112	0.069	0.059	0.07	0.072	0.34	0.099	0.583
Ca	0.006	0.005	0.004	0.002	0.005	0.006	0.005	0.002	0.008	0.005	0.005	0.001	0.004	0.01	0.017	0.02	0.005	0.007
Na	0.063	0.066	0.052	0.084	0.072	0.083	0.054	0.04	0.008	0.073	0.079	0.059	0.072	0.066	0.048	0.038	0.07	0.038
K	1.936	1.871	1.925	1.895	1.848	1.854	1.938	1.91	1.949	1.885	1.879	1.922	1.942	1.849	1.684	1.73	1.907	1.845

Garnet was analyzed only in the medium-grained albite granite; chemical analyses, structural formulae, and end-member fractions are listed in Table 4. The analyzed garnet crystals are essentially homogeneous and unzoned. They are rich in FeO (12.1-13.6 wt.%) and MnO (27.9-29.7 wt.%) and are essentially on the join between spessartine (64.9-69.6 mol%) and almandine (29.0-33.4 mol%), with minor pyrope (0.5-1.4 mol%) and grossular (0.6-1.1 mol%). The chemical homogeneity and highly euhedral form suggest that the garnets are magmatic. Low MgO and high MnO in garnet indicate crystallization at a shallow depth (Patiño Douce, 1999).

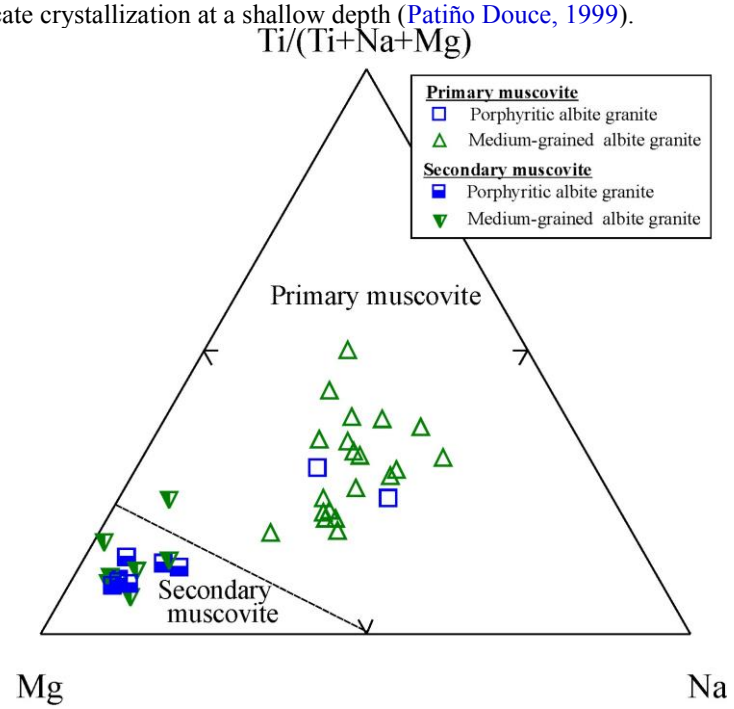

Fig. 5. Muscovite crystal chemistry.
Compositional fields for primary and secondary muscovite after Miller et al. (1981). Ti, Mg and Na = apfu.

Table 4. Microprobe anlayses of garnet in the medium-grained albite granite of Abu Dabbab pluton.

Sample No.	AD9				AD28			AD36				
Spot No.	#1	#2	#3	#4	#1	#2	#3	#1	#2	#3	#4	#5
SiO_2	36.690	36.395	36.332	36.342	36.146	36.756	36.337	36.06	36.578	36.342	36.417	36.194
TiO_2	0.145	0.127	0.053	0.043	0.088	0.046	0.108	0.078	0.091	0.082	0.117	0.066
Al_2O_3	20.474	20.413	20.510	20.255	20.464	19.832	20.235	20.402	20.138	20.247	20.464	20.461
Cr_2O_3	0.027	0.041	0.014	0.033	0.032	0.028	0.023	0.022	0.032	0.027	0.036	0.019
FeO	12.934	13.115	13.485	12.930	12.054	12.708	13.553	12.689	12.926	13.217	12.502	13.084
MnO	28.218	28.013	27.865	28.147	29.744	28.408	28.253	28.925	28.211	28.222	28.985	28.391
MgO	0.281	0.277	0.332	0.125	0.173	0.164	0.260	0.187	0.215	0.192	0.224	0.258
CaO	0.221	0.323	0.242	0.195	0.244	0.329	0.255	0.211	0.346	0.225	0.238	0.213
Na_2O	0.02	0.035	0.019	0.026	0.035	0.033	0.028	0.036	0.032	0.032	0.024	0.03
Total	99.01	98.74	98.85	98.10	98.98	98.30	99.05	98.61	98.569	98.586	99.007	98.716
Structural formula based on 12 oxygens												
Si	3.047232742	3.031806462	3.021725821	3.050057759	3.007499199	3.079927799	3.021466998	3.011356882	3.054475541	3.035703427	3.026982496	3.01693644
Ti	0.009058481	0.007957799	0.003315668	0.002714546	0.005507537	0.002899343	0.006754948	0.0048996	0.005715939	0.005152213	0.007315114	0.004138119
Al	2.004085523	2.004113085	2.010421166	2.003489749	2.006741539	1.958549012	1.983022457	2.008005445	1.981931637	1.993273244	2.004711622	2.010074118
Cr	0.00177295	0.00270034	0.000920595	0.002189717	0.002105087	0.001855005	0.001512068	0.00145256	0.002112718	0.001783155	0.002365828	0.001252155
Fe^{3+}	-0.118440919	-0.086341947	-0.06142474	-0.111224075	-0.034860098	-0.126058302	-0.040978417	-0.041970968	-0.104427314	-0.076767679	-0.075672668	-0.053475392
Fe^{2+}	1.016793387	1.000000742	0.999359638	1.018738963	0.873609951	1.016582025	0.98343254	0.92814679	1.007113595	1.000060377	0.944715601	0.965541059
Mn	1.985040036	1.976534953	1.962953106	2.000858975	2.096185804	2.016220746	1.989841493	2.045949925	1.9953556	1.996748796	2.040629568	2.004450775

Mg	0.03479147	0.034399178	0.041163508	0.015639318	0.021458528	0.020486355	0.032229286	0.023280197	0.026764781	0.023908938	0.027756347	0.03205958
Ca	0.01966633	0.028829387	0.021565238	0.017535049	0.021752453	0.029538016	0.022718628	0.01887957	0.030957504	0.020137529	0.021196094	0.019023145
End-members												
Almandine	33.27	32.90	33.04	33.37	28.99	32.98	32.48	30.77	32.91	32.89	31.13	31.96
Spessartine	64.95	65.02	64.89	65.54	69.57	65.40	65.71	67.83	65.20	65.66	67.25	66.35
Pyrope	1.14	1.13	1.36	0.51	0.71	0.66	1.06	0.77	0.87	0.79	0.91	1.06
Grossular	0.68	0.99	0.74	0.61	0.73	1.02	0.77	0.64	1.07	0.69	0.73	0.65

5 Whole rock geochemistry

5.1 Geochemical characteristics

The whole-rock chemical analyses of the ADAG samples and their calculated normative mineral compositions are listed in Tables 5 and 6. The albite granite samples vary significantly in their silica contents (72.3-78.4 wt.%) but all have high differentiation index (96-99), high abundance of total alkalis (Na_2O+K_2O = 7.5-9.8 wt.%), and Na_2O/K_2O ratios ranging between 1.8 and 2.7. The lowest SiO_2 contents are observed in the porphyritic samples (72.3-73.9 wt.%). The cataclastic albite granite samples appear to have suffered alkali and albite loss, complemented by gains in SiO_2, assuming they began as typical albite granites. As expected, albitite samples show low SiO_2 (69.9-70.8) and K_2O (0.2-0.5 wt.%) with high Na_2O (10.2-10.4 wt.%) and very high Na_2O/K_2O ratios (22.6-44.2). All ADAG samples have very low TiO_2, Fe_2O_3, MgO, and CaO. The two analyzed greisen samples, however, are comparatively rich in SiO_2, Fe_2O_3 and MnO but depleted in Na_2O and K_2O compared with the other rock types. The greisen samples also have the lowest Na_2O/K_2O ratios (0.9-1.4).

The ADAG samples plot well within the alkali granite field of the geochemical classification diagram of De la Roche et al. (1980) (Fig. 6), except the albitized samples plotted at the boundary between quartz syenite and syenite. Variations in major and trace element compositions of the suite, plotted against SiO_2 in Harker variation diagrams (Figs. 7, 8), show significant correlations despite obvious scatter. Excluding the cataclastic, greisenized and albitized granitic samples, there is a continuous trend through the porphyritic and non-porphyritic albite granite suite with no compositional gap. Al_2O_3, Fe_2O_3, CaO and K_2O decrease with increasing SiO_2, while Na_2O and MnO slightly increase (Fig. 7). A number of trace elements vary by a factor of two or more in concentration within the suite. Some trace elements — notably Ga, Rb, Y, Li and Cs — are negatively correlated with SiO_2, mostly because they show higher concentrations in the (low-SiO_2) porphyritic albite granite unit. Other trace elements — including Sr, Ba, Hf, Th, Nb, Ta and Zr — are positively correlated with SiO_2, in this case mostly because they show higher concentrations in the (high-SiO_2) non-porphyritic unit (Fig. 8). The cataclastic albite granite samples show wide variation in their trace element contents (Table 5). The greisenized samples are rich in Sn and Li and depleted in Ba, Nb and Zn.

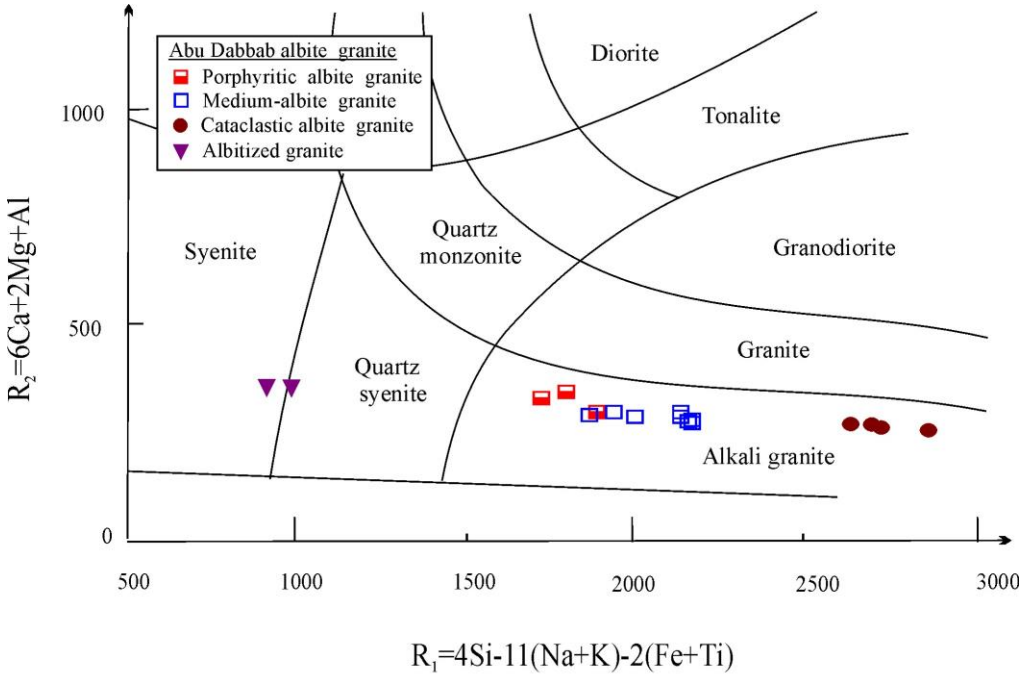

Fig. 6. Classification of Abu Dabbab albite granite using the R_1-R_2 diagram of De la Roche et al. (1980).

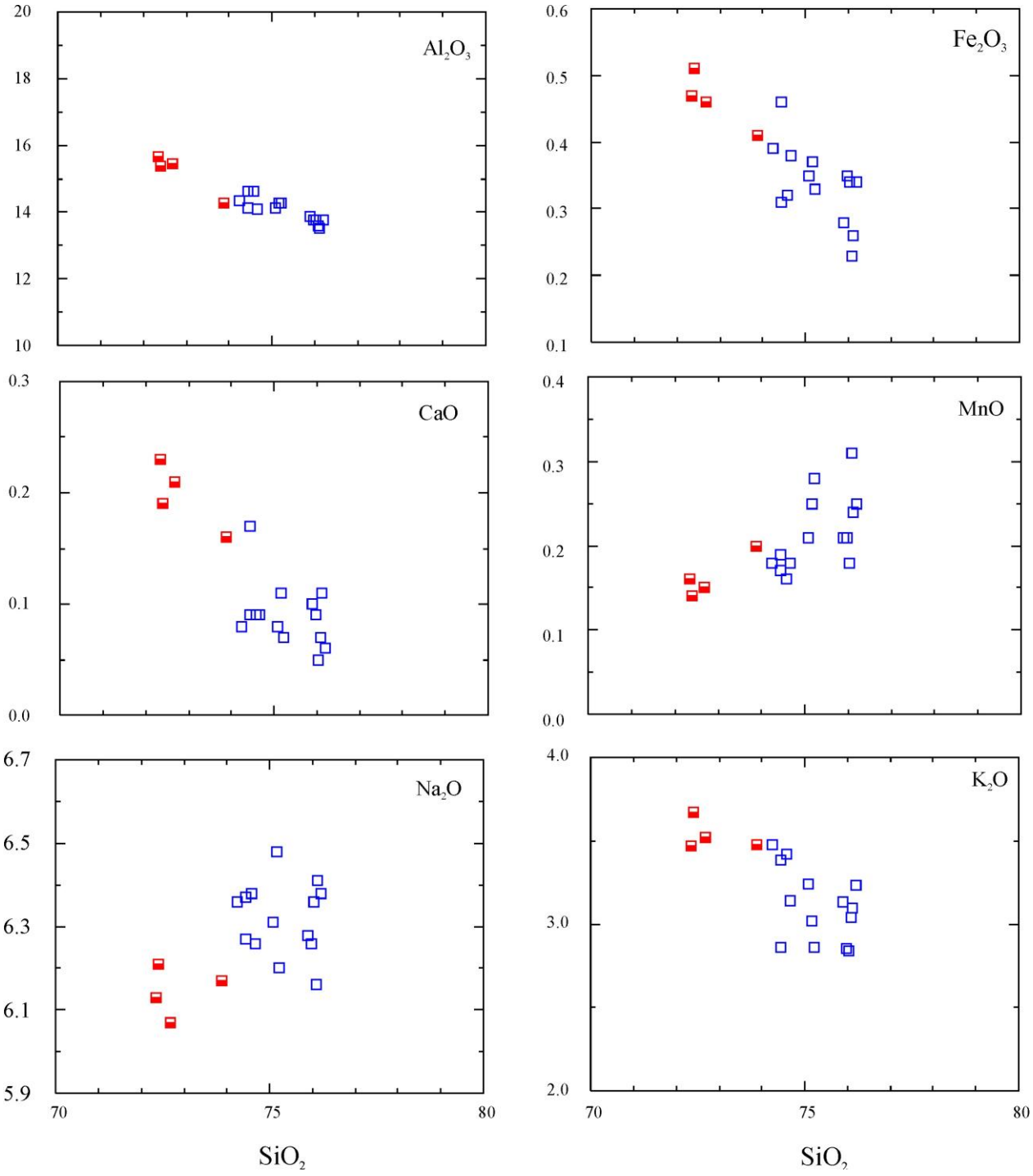

Fig. 7. Variation of major oxides against SiO_2.
Symbols as in Figure 6.

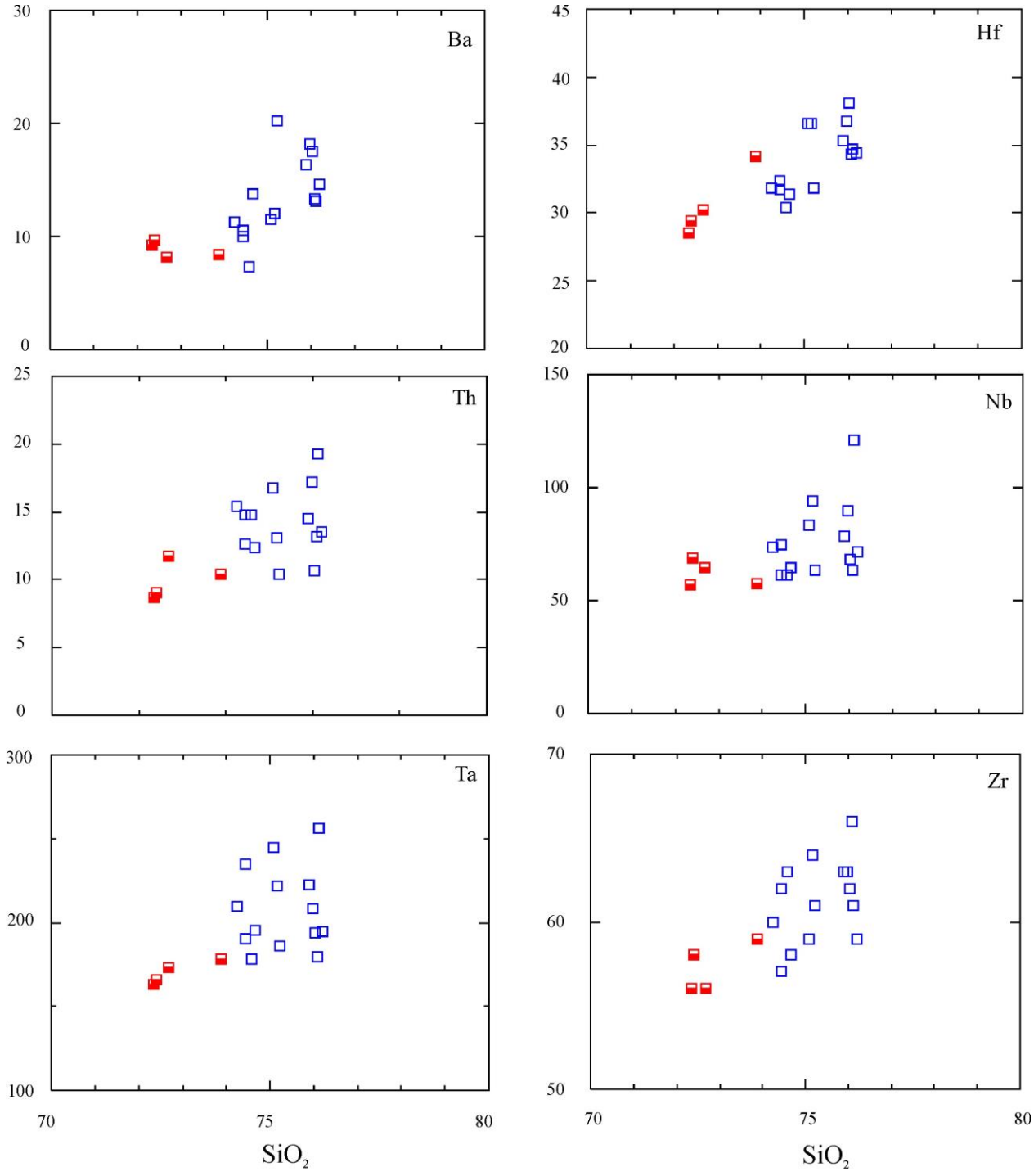

Fig. 8. Variation of some trace elements against SiO_2.
Symbols as in Figure 6.

Table 5 Major oxide and trace element contents of the Abu Dabbab albite granite.

Rock type	Porphyritic albite granite				Cataclastic albite granite					Albitized granite		Greisen	
Sample No	AD11	AD14	AD16	AD2	AD5	AD50*	AD53*	AD56*	AD61*	AD47*	AD49*	ADg-2	ADg-7
Major oxides (wt.%)													
SiO2	72.68	72.41	73.87	72.34	74.43	78.02	78.38	78.32	78.11	70.84	69.87	83.18	82.14
TiO2	0.02	0.02	0.01	0.02	0.02	0.01	0.01	0.01	0.01	0.01	0.01	0.02	0.02
Al2O3	15.44	15.36	14.28	15.65	14.12	13.31	12.56	13.24	13.36	17.87	18.22	10.71	11.64
Fe2O3	0.46	0.51	0.41	0.47	0.31	0.19	0.26	0.12	0.17	0.1	0.18	0.96	1.12
MnO	0.15	0.14	0.2	0.16	0.17	0.14	0.12	0.07	0.08	0.03	0.04	0.51	0.48
MgO	0.12	0.14	0.04	0.22	0.03	0.01	0.03	0.01	0.02	0.02	0.02	0.05	0.06
CaO	0.21	0.19	0.16	0.23	0.17	0.06	0.04	0.03	0.04	0.04	0.04	0.11	0.13
Na2O	6.07	6.21	6.17	6.13	6.27	5.18	4.91	5.54	5.72	10.38	10.16	1.24	1.09
K2O	3.52	3.67	3.48	3.47	3.38	2.84	2.61	2.26	2.29	0.46	0.23	1.32	0.76
P2O5	0.01	0.02	0.02	0.01	0.01	0.01	0.01	0.01	0.01	0.01	0.01	0.01	0.01
LOI	0.83	0.94	1.11	0.93	1.04	0.47	0.68	0.41	0.39	0.36	0.48	1.34	1.46
Total	99	99.06	99.51	*	99.86	100.24	99.61	100.22	100.6	100.15	99.05	99.45	99.71
Trace elements (ppm)													
Nb	64.4	68.6	57.8	57.3	61.6	49.6	56.4	91.3	86.2	126	137.5	34.3	41.5
Ta	173	166	178.1	163.5	190.6	87.4	107.6	167	217	266	294	194.2	216.7
Sn	761	844	882	748	895	765	873	886	960	427	447	2021	2151
Cs	3.7	3.2	2.5	3.7	2.7	1.48	2.07	1.16	1.09	0.35	0.4	3.9	4.3

Li	111	126	106	136	97	67	89	44	51	34	32	291.7	308.6
Ba	8	10	8	9	11	6	5	5	7	3	2	12	8
Sr	12	10	12	12	14	4	6	7	8	6	6	24	31
Rb	551	544	537	553	543	457	438	489	421	171.2	67	329	377
Zr	56	58	59	56	62	57	56	67	77	72	94.5	49	58
Zn	511	406	563	343	352	446	617	348	264	297	308.8	187	176
Ni	55	72	34	64	45	63	47	28	57	19	21.3	28	31
Cu	16	15	24	21	27	18	9	14	34	14	15	66	18
Th	11.7	9.1	10.4	8.7	12.6	6.2	8.4	29.3	36.7	9.7	24.6	17.7	20.1
U	6.1	6.3	6.2	6.1	6	4.6	5.3	7.8	9.1	9.4	11.2	5.5	4.8
Hf	30.2	29.4	34.2	28.5	31.7	24.6	23.5	37.1	46.5	51.5	52.4	23.2	21.6
Ga	129.5	132.4	124.6	127.8	114.5	96.5	93.7	89.2	84.5	101.2	144.1	99.4	114.1
Y	2.4	2.2	2.3	2.4	2	1.4	1.2	0.9	1.4	1.4	1.5	1.4	2.6
Geochemical parameters													
ASI	1.09	1.06	1.00	1.10	0.99	1.14	1.14	1.14	1.12	1.01	1.07	2.92	4.08
AI	0.91	0.94	0.99	0.90	1.01	0.89	0.89	0.89	0.91	1.00	0.95	0.33	0.23
Zr/Hf	1.9	2.0	1.7	2.0	2.0	2.3	2.4	1.8	1.7	1.4	1.8	2.1	2.7
K/Rb	53	56	54	52	52	52	49	38	45	22	28	33	17
K/Ba	3563	3141	3439	3097	2647	3803	4815	3474	2880	1193	796	945	809
Mg/Li	6.5	6.7	2.3	9.8	1.9	0.9	2.0	1.4	2.4	3.5	3.8	1.0	1.2
Ba/Rb	0.01	0.02	0.02	0.02	0.02	0.01	0.01	0.01	0.02	0.02	0.04	0.04	0.02

Rb/Sr	48	54	43	48	40	106	72	75	53	28	12	14	12

Table 6. Normative mineral compositions of the Abu Dabbab albite granites.

Rock type	Porphyritic albite granite				Cataclastic albite granite					Albitized granite		Greisen	
Sample No	AD11	AD14	AD16	AD2	AD5	AD50*	AD53*	AD56*	AD61*	AD47*	AD49*	ADg-2	ADg-7
Quartz	22.86	21.2	23.89	22.15	24.73	36.8	39.94	37.44	35.92	8.56	9.77	71.16	74.48
Corundum	1.2	0.8	0.0	1.3	-	1.6	1.6	1.7	1.4	0.2	1.2	7.2	9.3
Orthoclase	19.89	20.79	19.66	19.58	20.2	16.82	15.59	13.41	13.56	2.72	1.38	7.96	3.41
Albite	53.78	54.99	54.66	54.28	53.65	43.94	42	47.06	48.5	88.04	87.05	10.7	9.49
Anorthite	0.99	0.82	0.67	1.09	0.39	0.23	0.13	0.08	0.13	0.13	0.2	0.49	0.6
Acmite	-	-	-	-	-	-	-	-	-	-	-	-	-
Na-Metasilicate	-	-	-	-	-	-	-	-	-	-	-	-	-
Diopside	-	-	-	-	0.35	-	-	-	-	-	-	-	-
Diopside (Wo)	-	-	-	-	0.17	-	-	-	-	-	-	-	-
Diopside (En)	-	-	-	-	0.02	-	-	-	-	-	-	-	-
Diopside (Fs)	-	-	-	-	0.16	-	-	-	-	-	-	-	-
Hypersthene	1.07	1.18	0.9	1.35	0.5	0.45	0.56	0.26	0.36	0.2	0.32	2.08	2.29

Hypersthene (En)	0.3	0.35	0.1	0.55	0.06	0.02	0.08	0.02	0.05	0.05	0.05	0.13	0.15
Hypersthene (Fs)	0.77	0.82	0.8	0.8	0.44	0.42	0.49	0.23	0.31	0.15	0.27	1.95	2.14
Magnetite	0.14	0.15	0.14	0.15	0.11	0.08	0.09	0.05	0.06	0.03	0.05	0.34	0.37
Ilmenite	0.04	0.04	0.02	0.04	0.04	0.02	0.02	0.02	0.02	0.02	0.02	0.04	0.04
Apatite	0.02	0.04	0.04	0.02	0.02	0.02	0.02	0.02	0.02	0.02	-	0.02	0.02
Colour Index	1.26	1.36	1.06	1.54	1	0.54	0.67	0.32	0.44	0.25	0.39	2.46	2.7
Diff. Index	96.53	96.98	98.2	96.02	98.57	97.56	97.54	97.91	97.97	99.33	98.2	89.82	87.38

Most of the ADAG samples are peraluminous, with alumina saturation index [ASI = molar ratio $Al_2O_3/(CaO+Na_2O+K_2O)$] greater than unity (Table 5). The highest ASI values are observed in the samples rich in muscovite (the main aluminous mineral), especially greisen samples. Normative corundum reaches up to 1.7% in the albite granite; greisen samples have the highest normative corundum fractions (7.2-9.3%). Most ADAG samples have agpaitic index [AI = molar (Na+K)/Al] greater than 0.87 (0.89-1.04), as expected for alkaline rocks (Liégeois and Black, 1987; Liégeois et al., 1998). The low values of AI (0.23-0.33) in greisen samples reflect that high modal abundance of muscovite in these rocks. The very high Ga/Al ratios and elevated Nb concentrations of the ADAG samples place them firmly in the A-type group (Whalen et al., 1987; Eby, 1990), as shown on the discrimination diagrams of Whalen et al. (1987) (Fig. 9a, b). However, on the high-SiO_2 rock classification diagram of Sylvester (1989) (Fig. 9c), the samples plot in the highly fractionated calc-alkaline field. It is conceivable therefore that the ADAG and its A-type character represent the residual liquid after extensive fractional crystallization of an I-type calc-alkaline primitive melt (e.g., Collins et al., 1982; Clemens et al., 1986; Whalen et al., 1987; King et al., 1997). The ADAG shares many features of highly fractionated A-type granites worldwide, including high concentrations of total alkalis, Nb, and Ta alongside low concentrations of Ba, Zr and Sr (King et al., 1997; Wu et al., 2002; Dahlquist et al., 2014).

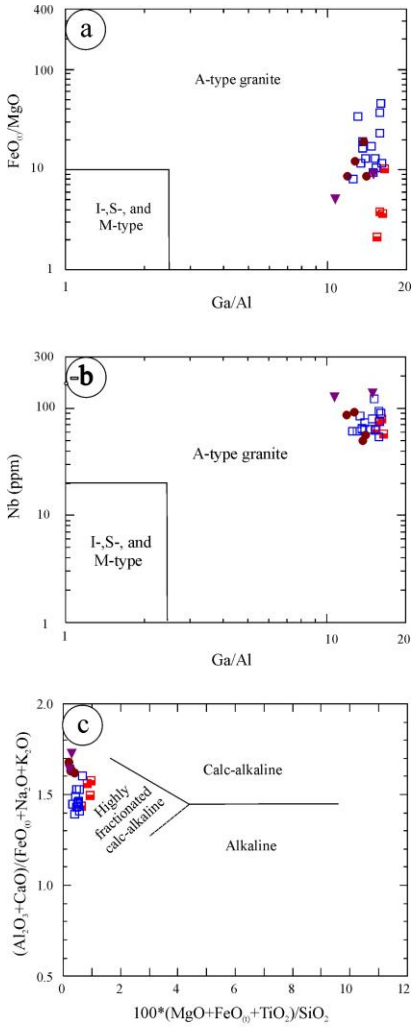

Figure 9

Fig. 9. Tectonic discrimination diagrams.
(a) Ga/Al vs. $FeO_{(t)}$/MgO diagram of Whalen et al. (1987), (b) Ga/Al versus Nb diagram of Whalen et al. (1987) and (c) Discrimination diagram of Sylvester (1989) for rocks with > 68 wt. % SiO_2. Symbols as in Figure 6.

5.2 Spider diagrams

Multi-element trace element patterns of the ADAG samples relative to mid-ocean ridge basalt (normalization values of Pearce, 1983) are shown in Fig. 10a. All albite granite samples (excluding cataclastic albite granite, albitite and greisen samples) display uniform and very similar spider diagrams characterized by both absolute depletion and negative anomalies in Sr, Ba, P, Ti, and Y alongside both absolute enrichment and positive anomalies of Rb, Th, Ta, Nb and Hf. Sn and Ga, not shown in the patterns, are also strongly enriched. The depletions in the patterns reflect extensive fractional crystallization of feldspars, apatite and Fe-Ti oxides. The enrichments, even in samples without obvious concentrations of rare minerals, reflect the rare-metal character of the albite granite.

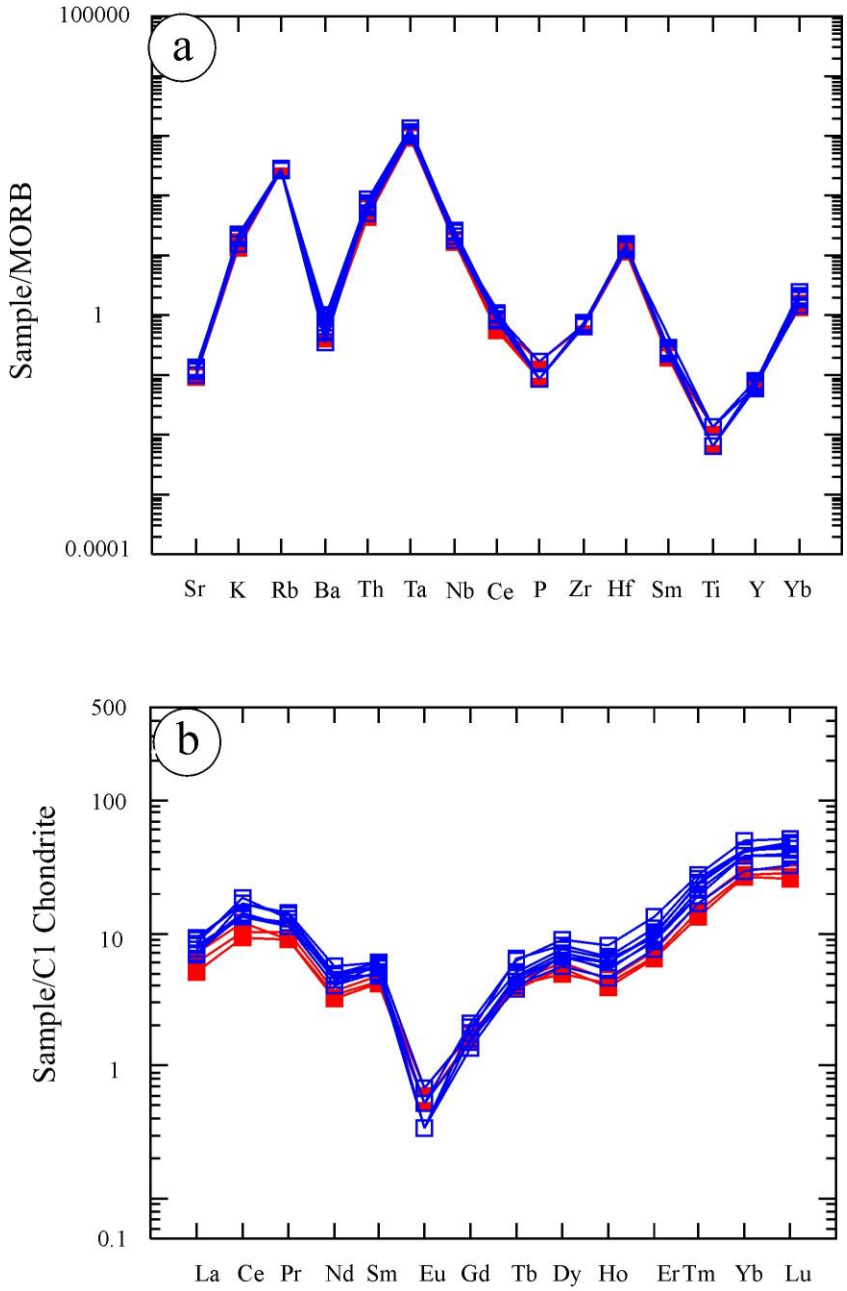

Figure 10

Fig. 10. Trace element patterns.
(a) Mid-ocean ridge basalt (MORB)-normalized trace element diagram and (b) chondrite-normalized rare earth element (REE) patterns for the ADAG. Normalization values in (a) from Pearce (1983) and in (b) from Evensen et al. (1978). Symbols as in Figure 6.

5.3 REE characteristics

Rare earth element concentrations of representative samples of the ADAG are given in Table 7 and their chondrite-normalized patterns (normalization of Evensen et al., 1978) are shown in Fig. 10b. The porphyritic samples have lower total REE (16-24 ppm) than the medium-grained samples (24-33 ppm), but all the measured patterns are nearly parallel with similar anomalies. They have high concentration of heavy rare earth elements (HREEs) relative to light rare earth elements (LREEs), reflected in very low values of $(La/Lu)_n$ (0.19-0.29). This feature is characteristic of rare-metal bearing granites in the Eastern Desert of Egypt (e.g. Hassanen et al., 1995; Abdalla, 2009; Abu El-Rus et al., 2017; Azer et al., 2019a, b). The depletion in LREE has been variously attributed to fractionation of accessory phases such as monazite (Mittlefehldt and Miller, 1983) or to scavenging by a fluorine-rich fluid (Webb et al.,1985).

Table 7. Rare earth element contents in Abu Dabbab albite granites.

Rock type	Medium-grained albite granite								Porphyritic albite granite		
Sample	AD5	AD9	AD20	AD23	AD33	AD36	AD39	AD44	AD11	AD16	AD2
La	1.7	2	1.8	2.2	1.9	2.1	1.8	1.6	1.4	1.7	1.2
Ce	8.4	11.1	8.1	10.1	8.2	10.2	8.6	10.2	6.3	7.4	5.7
Pr	1.07	1.21	1.06	1.32	1.13	1.28	1.05	1.35	0.96	0.84	0.86
Nd	1.9	2.19	2.2	2.3	2.1	2.3	1.9	2.6	1.7	1.5	1.6
Sm	0.88	0.82	0.74	0.91	0.75	0.87	0.78	0.91	0.72	0.64	0.67
Eu	0.02	0.03	0.03	0.02	0.02	0.02	0.02	0.04	0.04	0.03	0.03
Gd	0.28	0.43	0.31	0.4	0.33	0.33	0.33	0.36	0.35	0.32	0.33
Tb	0.15	0.23	0.17	0.19	0.18	0.16	0.14	0.24	0.16	0.15	0.14
Dy	1.41	2.25	1.69	1.94	1.79	1.67	1.72	2.03	1.52	1.26	1.36
Ho	0.26	0.45	0.34	0.36	0.34	0.31	0.3	0.38	0.25	0.24	0.22
Er	1.27	2.21	1.58	1.51	1.61	1.45	1.49	1.78	1.23	1.09	1.07
Tm	0.42	0.69	0.61	0.48	0.59	0.49	0.53	0.65	0.43	0.37	0.34
Yb	4.97	8.35	7.23	6.41	6.94	6.46	6.48	7.23	5.14	4.61	4.56
Lu	0.81	1.32	1.21	1.01	1.17	0.98	0.98	1.09	0.76	0.73	0.66
Eu*	2.80	3.35	2.70	3.40	2.81	3.02	2.86	3.23	2.83	2.55	2.89
Eu/EU*	0.12	0.15	0.19	0.10	0.12	0.11	0.12	0.21	0.24	0.20	0.24
(La/Yb)n	0.23	0.16	0.17	0.23	0.19	0.22	0.19	0.15	0.18	0.25	0.18
((La/Sm)n	1.22	1.54	1.54	1.53	1.60	1.52	1.46	1.11	1.23	1.68	1.12

(Gd/Lu)n	0.04	0.04	0.03	0.05	0.03	0.04	0.04	0.04	0.06	0.05	0.06
(La/Lu)n	0.22	0.16	0.15	0.22	0.17	0.22	0.19	0.15	0.19	0.24	0.18

The REE patterns of the albite granite show strongly negative Eu anomalies [(Eu/Eu*)=0.10-0.24], especially in the medium-grained unit. Together with the large depletions in Ba (5-20 ppm) and Sr (10-14 ppm), these are characteristic features of melts residual to extensive removal of feldspars by magmatic differentiation (Hanson, 1980; Möller and Muecke, 1984; Lee et al., 2013; Azer, 2013) under conditions reducing enough to stabilize some of the Eu as Eu^{2+} (Hanson, 1978; McKay, 1989). These elements are also fluid-mobile. Late-stage fluid transport can lead to very low (Eu/Eu*) (Irber, 1999; Jahn et al., 2001; Zhao et al., 2002) and also mobilize Sr and Ba as well as Ca. However, the depth of the Eu anomaly is not clearly correlated with the Sr, Ba, or Ca concentrations.

The normalized REE patterns of the ABAG show elevated (Ce, Pr), (Tb, Dy), and (Tm, Yb) relative to the neighboring REE, in some cases by up to a factor of two. This may be an expression of the REE tetrad effect (Irber et al., 1994; Irber, 1999), a quantum-mechanical effect causing deviations from the otherwise smooth, ionic radius-controlled, trend in behavior across the lanthanide contraction series. The tetrad effect has been noted in several similar alkaline granites of the ANS (Katzir et al., 2007; Azer, 2013). This effect is typical of transitional magmatic–hydrothermal systems and is often found in highly evolved volatile-rich granites. According to Irber (1999) and Jahn et al. (2001), it is unlikely that mineral fractionation alone could generate the tetrad effect in evolved granites. Rather, these authors emphasized the importance of exchange with aqueous fluid during the final stages of granite crystallization. A fluid-mobilization theory for the tetrad REE effect in the present suite is supported by depletions and anomalies in other fluid mobile elements, including very low ratios of Eu/Eu* (0.10-0.24), (La/Yb)n (0.16-0.25), La/Nb (0.02-0.03), Zr/Hf (1.4-2.7), and K/Rb (17-56) together with very high K/Ba ratios (1175-3889). Anomalously low Eu concentrations are common in granitic rocks showing the REE tetrad effect and these may have a common cause, namely fluid mobilization (Irber, 1999; Yang et al., 2011; Lee et al., 2013).

6 Discussion

At least fifteen different post-collisional intrusions in the Eastern Desert of Egypt have been described as rare-metal granites (Fig. 2a) (e.g. Helba et al., 1997; Küster, 2009; El Hadek et al., 2016; Abu El-Rus et al., 2017). Despite the economic significance of these granites, their origin and evolution are not yet well-understood. Since the ADAG has all the common characteristics of these rare-metal bearing granites — Rb > 500 ppm, Li > 100 ppm, K/Rb < 100, Mg/Li < 30, Ba/Rb < 0.5 and Rb/Sr > 10 (Beus, 1968; Tischendorf, 1977; Olade, 1980; Ramsay, 1986; Srivastava et al., 2007; Zhu et al., 2006, 2018) — we will develop the ADAG as a case study of the post-collisional rare-metal granites of the ANS. We apply our data from the present study to assess the tectonic setting, magmatic sources, and processes responsible for generation and evolution of the ADAG and, by extension, the rare-metal granites of the ANS as a group.

6.1 Tectonic setting of the ADAG

The ADAG represents the youngest igneous activity in the study area. Our field work and petrographic studies demonstrate that the ADAG is undeformed and unmetamorphosed, excepting local brittle deformation along shear zones associated with emplacement and along the Najd fault system. A conspicuous feature of the ADAG is an absence of mafic microgranular enclaves or dykes, in contrast to the abundance of such features in the surrounding country rocks. The ADAG shares geochemical characteristics with anorogenic, post-collisional igneous rocks, including alkaline character and high Ga/Al, Nb, Y and Ga along with low MgO, CaO, Sr, Ba and Zr. Also, the ADAG samples have marked enrichment in HFSEs including REEs, with pronounced negative Eu anomalies. These geochemical features are typically characteristic of within-plate magmatism (Whalen et al. 1987; Eby 1990, 1992).

We can confidently conclude that the ADAG was emplaced in a post-orogenic stable intraplate environment, even though most conventional immobile-element tectonic discrimination diagrams (e.g., Pearce et al., 1984, Harris et al., 1986) are not suitable for the ADAG because of its highly anomalous trace element characteristics. The within-plate tectonic setting of the ADAG is substantiated by plotting the data on the multicationic diagram of Batchelor and Bowden (1985); the ADAG samples appear in the anorogenic and post-orogenic granitic fields (Fig. 11).

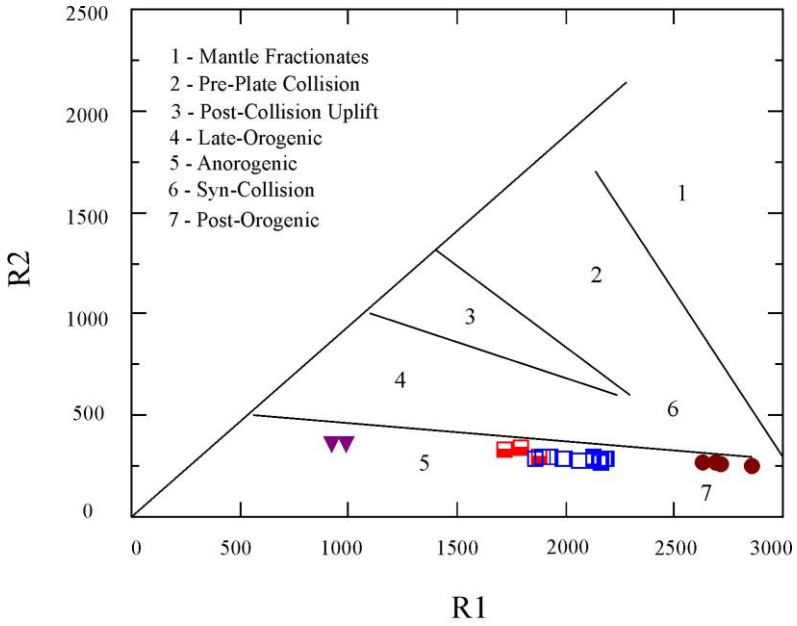

Figure 11

Fig. 11. The tectonic discrimination (R_1–R_2) of Batchelor and Bowden (1985).

6.2 Source magma and geodynamic model

Rare-metal granites are unusual mineralized granitic rocks that feature significant enrichments of one or more of the following elements: Zr, Ta, Nb, Hf, Li, Be, W, Sn, U, Th and REE. Several petrogenetic models have been proposed for these granites; they can be divided rather neatly into theories invoking the action of metasomatic-hydrothermal fluids on granitoids (e.g. Demange, 1975; Chauris, 1985; Cathelineau, 1988; Rugless and Pirajno, 1996; Antipin et al., 2018) and those emphasizing a magmatic origin as a variant of A-type magma (e.g. Schwartz, 1992; Chaudhri et al., 2003; Sklyarov et al., 2016). Experimental results on granitic systems (e.g., Pichavant and Manning, 1984; London, 1987) have been interpreted as support for the magmatic theory of albite granites and rare-metal pegmatites, despite their unusual compositions (Kovalenko and Kovalenko, 1984; Černý, 1992).

Interpretations of the ADAG genesis in particular are diverse and are not yet adequately addressed. Mohamed (1993, 2013) adopted a metasomatic-hydrothermal model for modification of a highly fractionated primary granite. Renno et al. (1993), by contrast, proposed a magmatic model emphasizing an enriched parental magma derived from remelting of lower crust. Tkachev (2011) concluded that the source of the Abu Dabbab and Nuweibi rare-metal granites were in deeply buried parts of the oldest orogenic belts within the ANS, remobilized and emplaced along late-orogenic structures into juvenile Neoproterozoic rocks.

In the Eastern Desert of Egypt, all the rare-metal bearing granites are A-type rocks. However, large differences in major and trace element concentrations and isotope ratios among various A-type granitic rocks in the ANS demand that a variety of processes and sources were responsible for their origins (e.g. Jarrar et al., 2008; Eyal et al., 2010; Ali et al., 2014, 2015; Azer et al., 2014; Gahlan et al., 2016; Khalil et al., 2018; Abdallah et al., 2019). Theories for A-type granites in the ANS also fall into two distinct groups, those invoking extensive fractional crystallization of mantle-derived mafic magmas (e.g. Stern and Gottfried, 1986; Bonin, 2007; Stern and Voegeli, 1987; Beyth et al., 1994; Kessel et al., 1998; Mushkin et al., 2003; Jarrar et al., 2008) and those based on partial melting of various crustal sources (e.g., Clemens et al., 1986; Creaser et al., 1991; King et al., 1997; Abdel-Rahman, 2006; Farahat et al., 2007; Ali et al., 2009), plus some models that are hybrids of these end-members. A mid-crustal source is commonly invoked in crustal-melting models (e.g. Abdel-Rahman, 2006; Farahat et al., 2007; Eyal et al., 2010; Sherif et al., 2013). Generally, A-type felsic rocks derived by fractional crystallization of mantle-derived magma should be expected to exhibit a continuous compositional trend from mafic through intermediate to felsic rocks

(Kessel et al., 1998; Mushkin et al., 1999), though of course rocks representing all parts of the sequence may not be exposed. Nevertheless, a partial melting process better explains the scarcity of mafic rocks and the absence of intermediate compositions among A-type plutonic rocks in the region.

The primary evidence supporting a mantle origin has been the radiogenic isotope signatures of A-type rocks of the ANS, including positive $\varepsilon_{Nd}(t)$ and $\varepsilon_{Hf}(t)$ values of +7 to +8 (Morag et al., 2011). However, these signatures can also be attributed to partial melting of juvenile crust (e.g. Haapala et al., 2007, Farahat et al., 2007) such as re-melting of island-arc crust from the last orogenic stages of assembly of the ANS. Such mid-crustal sources would not have had time to evolve radiogenic isotope signatures before being sampled by the A-type post-orogenic activity. Moreover, Be'eri-Shlevin et al. (2009) interpreted the elevated $\delta^{18}O$ of some A-type granites of the northern ANS as evidence of derivation from crustal reservoirs. The highly evolved nature of ADAG and the absence of any mafic or intermediate magmatic rocks argue against their formation from mantle-derived magma. The absence of enclaves further argues against hybridization models.

Melting of crustal rocks requires elevated temperatures, which may develop during large-scale strike-slip movements along reactivated transcurrent faults. Therefore, the emplacement of the ADAG most probably occurred along Pan-African fractures re-activated by relaxation after the termination of the Pan-African orogeny. The extensive erosion that preceded the emplacement of the ADAG, together with the crustal rupture and unusually thin crust in Egypt (about 35 km; Mechie and Prodehl, 1988), may have caused pressure release at depth and influx of volatiles into the crust from deeper sources. High temperature, decreasing pressure, and volatile addition all promote partial melting of the crust.

Turning to differentiation of the ADAG magmatic suite, the geochemical characteristics of the pluton indicate evolution from a common parental magma by extensive fractional crystallization and fluid fractionation. However, the formation of such an albite-rich magma is puzzling because phase relations in the haplogranitic system Qz-Ab-Or (Holtz et al., 1992) do not allow liquid of albite granite composition to form by crystal fractionation of dry granitic magma. In this case, though, the low K/Rb ratios (22-56) and other evidence indicate crystallization from a silicate melt saturated with and equilibrating with an aqueous fluid phase (e.g., Irber, 1999; El Maghraoui et al., 2002; London et al., 2012). Elevated water pressure shifts the location of the granite minimum towards the albite apex of the Qz-Ab-Or ternary (Fig. 12) (Winkler et al., 1975). Furthermore, fluorite in some ADAG samples testifies to elevated fluorine in the magmatic fluids, which also shifts minimum melt compositions towards albite (Manning, 1981).

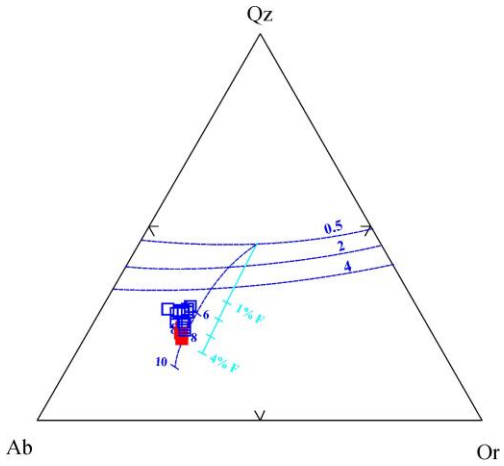

Figure 12

Fig. 12. Normative composition of the NAG samples plotted in Qz–Ab–Or projection.
Dashed lines show the quartz-alkali feldspar cotectics and the trace of the water-saturated minimum melt compositions in the haplogranite system at total pressure ranging from 0.5 to 10 kbar (Holtz et al., 1992; Winkler et al., 1975). Solid cyan line shows the trace of the minimum melt composition at 1 kbar with excess H_2O and increasing fluorine (F) content up to 4 wt.% F (Manning, 1981).

The geochemical variations within the ADAG suite are challenging to assign to specific differentiation processes because of poor correlations between SiO_2 and major and trace element concentrations (Figs. 7, 8) and among various trace element concentrations and ratios (Table 5). Overall, it is clear from the negative P and Ti anomalies of the whole suite that there was a major role for apatite and Fe-Ti oxides, either as residual phases in the crustal source area or during fractionation at deeper levels than presently exposed in the pluton. Likewise, very pronounced negative Eu anomalies and strong depletion in Ba and Sr imply residual or extensively fractionated feldspar, though these elements may also be strongly overprinted by fluid-related processes (see below).

6.3 Evidence for magmatic vs. metasomatic effects

Rare-metal bearing granites in the Eastern Desert of Egypt have been attributed variously to magmatic processes (Asran, 1985; Mohamed, 1993; Helba, 1994; Jahn, 1996; Helba et al., 1997; Arslan et al., 1997; Renno, 1997; Abou El Maaty and Ali Bik, 2000) or to post-magmatic high-temperature metasomatism (Sabet et al., 1976; El-Tabal, 1979; Riad, 1979; Kamel and E1 Tabbal, 1980). The ADAG in particular has likewise been assigned by different authors to either magmatic (Asran, 1985; Mohamed, 1993; Jahn, 1996; Renno, 1997) or metasomatic origins (Sabet et al.,1976; Kamel and E1 Tabbal, 1980). In fact, the distinction between magmatic and metasomatic processes may not be as absolute as once thought (Lundstrom, 2016; Azer et al., 2019a).

A number of observations support the preservation of important magmatic signatures in the ADAG despite the action of metasomatic processes. Certainly, the overall enrichment in fluid-immobile rare metals, characterizing the entire intrusion, was a primary magmatic feature. Only limited late stage redistribution of these metals is likely, and this may have been dominated by gravitational settling at high melt fractions. The sharp intrusive contacts and chilled margins of the ADAG against the country rocks indicate their magmatic origin. The coexistence of primary albite, muscovite (Fig. 5), and K-feldspars as euhedral to subhedral crystals argues for a magmatic origin. Likewise, primary muscovite and feldspars are included in subhedral to euhedral quartz phenocrysts of rather uniform size. Although “snowball" quartz has been interpreted as both a metasomatic (Beus, 1982; Müller and Seltmann, 1999) and a magmatic (Vance, 1969; Pollard, 1989; Schwartz, 1992; Müller and Seltmann, 1999) feature, the ADAG examples appear to be magmatic textures.

Although the main phases of the ADAG are primarily magmatic, the effects of hydrothermal fluids and extensive replacement by secondary minerals become dominant in marginal zones along the southern boundary of the magma chamber. Such extensive metasomatism is mainly manifested by the development of greisen, stockscheider pegmatites and quartz veins along fracture systems in the albite granite. During greisenization, primary minerals (albite, perthite and muscovite) are consumed and a new generation of minerals forms, including quartz, mica, topaz, fluorite, cassiterite and wolframite. Chemically, comparison to fresh samples indicates that greisenization is accompanied by dramatic increases in SiO_2, Fe_2O_3, MnO, Sn and Li complemented by significant losses of Na_2O, K_2O, Ba, Nb and Zn. The chemical and mineralogical changes are consistent. Increasing SiO_2 reflects secondary quartz; decreasing alkalis reflect loss of feldspar; increases in Sn, Fe_2O_3 and MnO are hosted by cassiterite and wolframite. Alumina liberated by the destruction of feldspars was incorporated in secondary mica and topaz.

Additionally, the less obviously fluid-modified samples preserve mineralogical features indicating partial alteration and replacement under subsolidus conditions. These features include (i) partial replacement of microcline by albite with preservation of the original crystal habit of microcline, (ii) sparse alteration of albite crystals to sericite, muscovite and chlorite, (iii) overgrowth of secondary albite around K-feldspar, quartz and primary albite, and (iv) formation of amazonite. Some textural categories of muscovite, for example where it is seen replacing albite and K-feldspar, have chemistry attributable to secondary formation (Fig. 5). In addition, the existence of biotite relics within muscovite may indicate reaction of magmatic biotite with immobile Al released during hydrothermal breakdown of feldspars (Tao et al., 2014; du Bray, 1994). Hence, we interpret some muscovite in the medium-grained albite granite as a secondary phase, even though primary muscovite is present and the ADAG formed in a magmatic environment typical of muscovites in other peraluminous granitoids worldwide (Tao et al., 2014).

Chemically, the gradual decrease in REE concentrations from the lower medium-grained albite granite to the porphyritic type, and the ingrowth of a small tetrad effect anomaly probably both reflect leaching of the accessory minerals during post-magmatic fluid activity (Barboni and Bussy, 2013). Features such as anomalously low Eu, Sr, Ba, and K may also testify to leaching by late magmatic to post-magmatic fluid migration.

The Abu Dabbab granitic mass is distinguished into a medium-grained (hypabyssal) albite granite and a fine-grained porphyritic albite granite. We interpret this distinction in type and texture to reflect vertical zonation of the magma chamber, with the southern portion of the outcrop presently exposing a shallower level of emplacement and the northern portion a deeper level. The porphyritic albite granite represents the preserved remnants of the upper-level apex of the magma chamber whereas the medium-grained albite granite crystallized under deeper, subvolcanic conditions. The fine-grained matrix of porphyritic albite granite might be a result of pressure quenching related to opening of fractures and vigorous escape of volatiles. Accumulation of residual volatile-rich melt and exsolved fluids

in the apical part of the magma chamber produced stockscheider pegmatite, greisen and quartz veins that cut the peripheries of the granitic pluton of Abu Dabbab and its surrounding country rocks. Metasomatic activity by late- to post-magmatic fluids locally leached potassium and formed pure albitite salvages.

The mode of emplacement of the ADAG is very similar to the Tarr albitite in southern Sinai (Azer et al., 2010, 2019c) and the Nuweibi albite granite in the Eastern Desert of Egypt (Azer et al., 2019a), despite the obvious differences in their chemical compositions. Each of these intrusions is divided into hypabyssal and porphyritic varieties suggesting that a gradient in emplacement depth extending to very shallow crustal levels is preserved and exposed in each case. The boundary between the two phases in the ADAG and in the Nuweibi albite granite is gradational and the simultaneous crystallization of the two phases can be established with confidence. On the other hand, the boundary between hypabyssal and porphyritic albitites at Wadi Tarr is not clear and the temporal relationship between the two phases cannot be established. Notably, the marginal zones around the ADAG and the Nuweibi albite granite are quite similar, featuring pegmatite stocks, quartz veins and greisen, whereas the margins of the Tarr albitite are surrounded by volcanic breccias and fenitization zones. The suggested model for the emplacement of the ADAG intrusion is shown in Fig. 13.

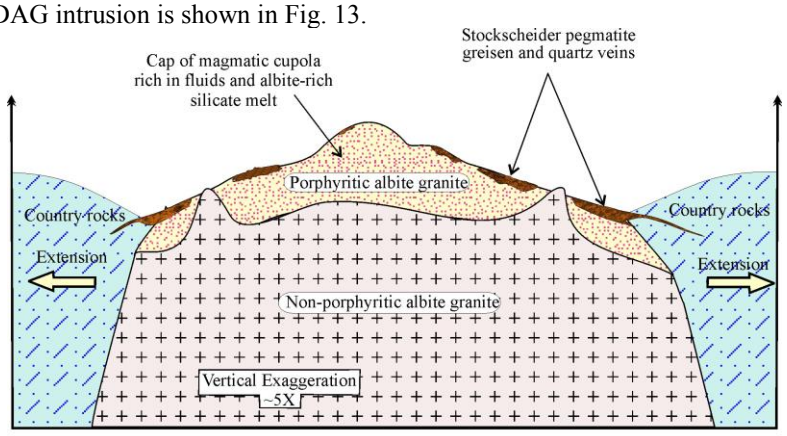

Figure 13

Fig. 13. Suggested model for the emplacement of the ADAG intrusion in a magmatic cupola (adapted from Azer et al. 2019a).

7 Summary

The Abu Dabbab albite granite is an ellipsoidal intrusive stock emplaced into metamorphic country rocks with development of a contact metamorphic aureole of amphibolite and hornfels. The intrusion itself is unmetamorphosed. The A-type ADAG is typical in many ways of the rare-metal bearing granites of the northern ANS, emplaced in the shallow crust during the post-collisional phase of ANS assembly. It is undeformed except in marginal zones due to shear upon emplacement or due to later motion on the ~600 Ma Najd Fault System. The main mass of the ADAG is distinguished into two varieties with the same mineralogical composition: medium-grained albite granite and fine-grained porphyritic albite granite. The latter is less common, exposed only in the southern portion of the outcrop, and represents a preserved remnant of the shallowly-emplaced apex of the magma chamber.

The ADAG consists essentially of quartz and albite with interstitial K-feldspars and muscovite. Primary albite was the liquidus mineral. The samples host numerous accessory minerals including Fe-Ti oxides, allanite, zinnwaldite, apatite, cassiterite, tantalite-columbite, fluorite, topaz, titanite, zircon and garnet. The major and trace element compositions and petrographic observations clearly classify the ADAG as a mineralized granite. The Nb-Ta mineralization in the ADAG is visible in outcrop because it occurs in black patches with Fe-Mn oxides. The density of these patches and the grade of Nb-Ta ore increases towards the northern, more deeply-emplaced part of the outcrop area. The formation of marginal pegmatite, quartz veins, greisen and amazonite can be attributed to the accumulation of residual melts and fluids below the roof of the magma chamber and their migration into fractures extending into the country rocks.

The petrology and geochemistry of the ADAG are most consistent with generation by partial melting of the juvenile middle crust of the ANS followed by ascent and emplacement at the intersection of lineations of structural weakness. Late-stage metasomatism caused limited redistribution of rare metals, moderate recrystallization in the interior of the intrusion, and development of focused veins of greisen, amazonite and quartz veins along fracture systems near the apex of the magma chamber.

Acknowledgments

The authors extend their appreciation to the Deanship of Scientific Research at King Saud University for funding this work through research group number RG-1439-037.

References

Abdalla, H.M., 2009. Mineralogical and Geochemical Characterization of Beryl- Bearing Granitoids, Eastern Desert, Egypt. Metallogenic and Exploration Constraints. *Resource geology*, 59(2): 121-139.

Abdallah, S.E., Azer, M.K., and El Shammari, A.S., 2019. Petrological and geochemical evolution of Ediacaran rare-metal bearing A-type granites from Jabal Aja complex, northern Arabian Shield, Saudi Arabia. *Acta Geologica Sinica*, (in press).

Abdel-Rahman, A.M., 2006. Petrogenesis of anorogenic peralkaline granitic complexes from eastern Egypt. *Mineralogical Magazine*, 70: 27-50.

Abou El Maaty, M.A., and Ali Bik, M.W., 2000. Petrology of alkali feldspar granites of Nuweibi and Gebel El-Mueilha, central Eastern Desert, Egypt. *Egyptian Journal of Geology*, 44: 127-148.

Abu El-Rus, M.A., Mohamed, M.A., and Lindh, A., 2017. Mueilha rare metals granite, Eastern Desert of Egypt: An example of a magmatic-hydrothermal system in the Arabian-Nubian Shield. *Lithos*, 294–295: 362–382.

Ali, B.H., Wilde, S.A., and Gabr, M.M.A., 2009. Granitoid evolution in Sinai, Egypt, based on precise SHRIMP U-Pb zircon geochronology. *Gondwana Research*, 15: 38-48.

Ali, K.A., Azer, M.K., Gahlan, H.A., Wilde, S.A., Samuel, M.D., and Stern, R.J., 2010. Age constraints on the formation and emplacement of Neoproterozoic ophiolites along the Allaqi-Heiani suture, South Eastern Desert of Egypt. *Gondwana Research*, 18: 583-595.

Ali, K.A., Jeon, H., Li, A., Andresen, S.-Q., Harbi, H.M., and Hegner, E., 2014. U–Pb zircon geochronology and Nd–Hf–O isotopic systematics of the Neoproterozoic Hadbadh Dayheen ring complex, Central Arabian Shield, Saudi Arabia. *Lithos*, 206 -207: 348-360.

Ali, K.A., Surour, A.A., Whitehouse, M.J. and Andresen, A., 2015. Single zircon Hf–O isotope constraints on the origin of A-type granites from the Jabal Al-Hassir ring complex, Saudi Arabia. *Precambrian Research*, 256: 131-147.

Antipin, V.S., Kuzmin, M.I., Odgerel, D., Kousch, L.V. and Perepelov, A.B., 2018. Geochemical Evolution and Ore-Bearing Metasomatic Rocks of the Baga-Gazryn Multiphase Massif of Rare-Metal Li–F Granites (Mongolia). In Doklady Earth Sciences (Vol. 483, No. 1, pp. 1468-1472). Pleiades Publishing.

Arslan, A.I., Helba, H.A., Khalil, S.O., and Morteani, G., 1997. Bedrock geochemical prospecting and ore potentiality of the rare metal-bearing granite at Nuweibi area, central Eastern Desert, Egypt. The Third Conference on Geochemistry, Alexandria University, Alexandria-Egypt, 3-4 September 1997, pp. 375-387.

Asran, M.H.A., 1985. Geology, petrography and geochemistry of the apogranites at Nuweibi and Abu Dabbab areas, Eastern Desert, Egypt. Unpubl. M.Sc. Thesis, Assiut University, Egypt, 149 pp.

Azer, M.K., 2013. Late Ediacaran (605-580 Ma) post-collisional alkaline magmatism in the Arabian–Nubian Shield: a case study of Serbal ring-shaped intrusion, southern Sinai, Egypt. *Journal of Asian Earth Sciences*, 77: 203-223.

Azer, M.K., Abdelfadil, K.M., Ramadan, A.A., 2019a. The Nuweibi rare-metal albite granite: a magmatic cupola above a highly fractionated post-collisional A-type granite pluton. *Journal of Geology* (Accepted with revisions).

Azer, M.K., Abdelfadil, K.M., Asimow, P.D., and Khalil, A.E.S., 2019b. Tracking the transition from subduction-related to post-collisional magmatism in the north Arabian-Nubian Shield: A case study from the Homrit Waggat area of the Eastern Desert of Egypt. *Geological Journal* (accepted).

Azer, M.K., Gahlan, H.A., Asimow, P.D., and Al-Kahtany, K.M., 2019c. The common origin and alteration history of the hypabyssal and volcanic phases of the Wadi Tarr Albitite Complex, southern Sinai, Egypt. *Lithos*, 324-325: 821-841.

Azer, M.K., Obeid, M.A., and Ren, M., 2014. Geochemistry and petrogenesis of late Ediacaran (580-605 Ma) post-collisional alkaline rocks from Katherina Ring complex, south Sinai., Egypt. *Journal of Asian Earth Sciences*, 93: 229-252.

Azer, M.K., Stern, R.J., and Kimura, J.-I., 2010. Origin of a Late Neoproterozoic (605±13 Ma) intrusive carbonate-albitite complex in Southern Sinai, Egypt. *International Journal of Earth Sciences*, 99: 245-267.

Barboni, M., and Bussy, F., 2013. Petrogenesis of magmatic albite granites associated to cogenetic A-type granites: Na-rich residual melt extraction from a partially crystallized A-type granite mush. *Lithos*, 177: 328–351.

Batchelor, R.A. and Bowden, P., 1985. Petrogenetic interpretation of granitoid rock series, using multicationic parameters. *Chemical Geology*, 48: 43–45.

Basta, F.F., Maurice, A.E., Betros, B.R., Azer, M.K., and El-Sobky, A., 2017. Intrusive Rocks of the Wadi Hamad Area, North Eastern Desert, Egypt: Change of Magma Composition with Maturity of Neoproterozoic Continental Island Arc and the Role of Collisional Plutonism in the Differentiation of Arc Crust. *Lithos*, 288-289: 248-263.

Be'eri-Shlevin, Y., Katzir, Y., and Whitehouse M., 2009. Post-collisional tectono-magmatic evolution in the northern Arabian-Nubian Shield (ANS): Time constraints from ion-probe U-Pb dating of zircon. *Journal of Geological Society of London*, 166: 71-85.

Beus, A.A., 1968. Geochemical specialization of magmatic complexes as criteria for the exploration of hidden complexes. *Proc. 23rd Internal Geological Congress Prague* 6, pp.101-105.

Beus, A.A., 1982. Metallogeny of Precambrian rare-metal granitoids. *Revista Brasileira de Geociências*, 12: 410-413.

Beyth, M., Stern, R.J., Altherr, R., and Kröner, A., 1994. The late Precambrian Timna igneous complex Southern Israel: Evidence for comagmatic-type sanukitoid monzodiorite and alkali granite magma. *Lithos*, 31: 103–124.

Bonin, B., 2007. A-type granites and related rocks: Evolution of a concept, problems and prospects. *Lithos*, 97: 1-29.

Boskabadi, A., Pitcairn, I.K., Broman, C., Boyce, A., Teagle, D.A.H., Cooper, M.J., Azer, M.K., Stern, R.J., Mohamed, F.H., and Majka, J., 2017. Carbonate alteration of ophiolitic rocks in the Arabian–Nubian Shield of Egypt: sources and compositions of the carbonating fluid and implications for the formation of Au deposits. *International Geology Review*, 59(4): 391-419.

Cathelineau, M., 1988. Accessory mineral alteration in peraluminous granites at the hydrothermal stage: A review. *Rendiconti della Società Italiana di Mineralogiae Petrologia*, 43: 499-508.

Černý, P., 1992. Geochemical and petrogenetic features of mineralization in rare-element granitic pegmatites in the light of current research. *Applied Geochemistry*, 7: 393–416.

Chaudhri, N., Kaur, P., Okrusch, M., and Schimrosczyk, A., 2003. Characterization of the Dabla granitoids, North Khetri Copper Belt, Rajasthan, India: evidence of bimodal anorogenic felsic magmatism. *Gondwana Research*, 6: 879-895.

Chauris, L., 1985. Premières données géochimiques sur les albitites metasomatiques des environs de Brest (Finistère, France). *Bulletin Societé Géologique de France*, 8: 885-889.

Clemens, J.D., Holloway, J.R., and White, A.J.R., 1986. Origin of an A-type granites: experimental constraints. *American Mineralogist*, 71: 317-324.

Collins, W.J., Beams, S.D., White, A.J.R., and Chappell, B.W., 1982. Nature and origin of A-type granites with particular reference to southeastern Australia. *Contribution to Mineralogy and Petrology*, 80: 189-200.

Creaser, R.A., Price, R.C., and Wormald, R.J., 1991. A-type granites revisited: Assessment of a residual-source model. *Geology*, 19: 163-166.

Dahlquist, J.A., Alasino, P.H., and Bello, C., 2014. Devonian F-rich peraluminous A-type magmatism in the proto-Andean foreland (Sierras Pampeanas, Argentina): geochemical constraints and petrogenesis from the western-central region of the Achala batholith. *Mineralogy and Petrology*, 108: 391–417.

De la Roche, H., Leterrier, J., Grandclaude, P., and Marchal, M., 1980. A classification of volcanic and plutonic rocks using R_1-R_2 diagrams and major-element analyses—its relationships with current nomenclature. *Chemical Geology*, 29: 183-210.

Demange, M., 1975. Zonation métasomatique autour des albitites de la région de Saint Chély d'Apcher (Lozère). *Bull Soc Fr Miner Cristallogr*, 98:186-190.

du Bray, E.A., 1994. Compositions of micas in peraluminous granitoids of the eastern Arabian shield. *Contributions to Mineralogy and Petrology*, 116: 381–397.

Eby, G.N., 1990. The A-type granitoids: A review of their occurrence and chemical characteristics and speculations on their petrogenesis. *Lithos*, 26: 115-134.

Eby, G.N., 1992. Chemical subdivisions of the A-type granitoids: petrogenesis and tectonic implications. *Geology*, 20: 641–644.

El Hadek, H.H., Mohamed, M.A., El Habaak, G.H., Bishara, W.W., and Ali, K.A., 2016. Geochemical Constraints on Petrogenesis of Homrit Waggat Rare Metal Granite, Egypt. *International Journal of Geophysics and Geochemistry*, 3(4): 33-48.

El Maghraoui, M., Joron, J.L., Raimbault, L., and Treuil, M., 2002. Element mobility during metasomatism of granitic rocks in the Saint-Chély d'Apcher area (Lozère, France). *Environment International*, 28: 349–357.

El-Tabal, H.K., 1979. Mineralogical studies on some rare metal apogranites from Nuweibi and Abu Dabbab areas, Eastern Desert, Egypt. MSc thesis, Al-Azhar University, Cairo, pp 112.

Evensen, N.M., Hamilton, P.J., and O' Nions, R.K., 1978. Rare earth abundances in chondritic meteorites. *Geochimica et Cosmochimica Acta*, 42: 1199-1212.

Eyal, M., Litvinovsky, B., Jahn, B.M., Zanvilevich, A., and Katzir, Y., 2010. Origin and evolution of post-collisional magmatism: Coeval Neoproterozoic calc-alkaline and alkaline suites of the Sinai Peninsula. *Chemical Geology*, 269: 153-179.

Farahat, E.S., Mohamed, H.A., Ahmed, A.F., and El Mahallawi, M.M. 2007. Origin of I- and A-type granitoids from the Eastern Desert of Egypt: implications for crustal growth in the northern Arabian–Nubian Shield. *Journal of African Earth Sciences*, 49: 43-58.

Gahlan, H.A., Azer, M.K., Asimow, P.D., and Al-Kahtany, K., 2016. Late Ediacaran post-collisional A-type syenites with shoshonitic affinities, northern Arabian-Nubian Shield: A possible mantle-derived A-type magma. *Arabian Journal of Geosciences*, 9: 613(doi:10.1007/s12517-016-2629-x).

Haapala, I., Frindt, S., and Kandara, J., 2007. Cretaceous gross spitzkoppe and klein spitzkoppe stocks in Namibia: topaz-bearing A-type granites related to continental rifting and mantle plume. *Lithos*, 97: 174-192.

Hanson, G.N., 1978. The application of trace elements to the petrogenesis of igneous rocks of granitic composition. *Earth planetary Sciences and letters*, 38: 26-43.

Hanson, G.N., 1980. Rare earth elements in petrogenetic studies of igneous systems. *Annual Review of Earth and Planetary Sciences*, 8: 371-406.

Harris, N.B., Pearce, J.A., Tindle, A.G., 1986. Geochemical characteristics of collision-zone magmatism. In: Coward, M.P. and Ries A.C. (eds) collision tectonics. *Journal of Geological Society, London, Special Publication,* 19: 67-81.

Hassanen, M.A., Saad, N.A., and Khalefa, O.M., 1995. Geochemical aspects and origin of Tin-bearing granites in the Eastern Desert, Egypt. *Acta Mineralogica-Petrographica*, XXXVI: 55-72.

Heikal, M.Th.S., Gomaa, S.R., Abd El Monsef, M., Taha, A.A., Top, G., Mahmoud, K.R., and El- Mansi, M.M., 2018. Insight on Radiological Risk Assessment and its Statistical Evaluations for Abu Dabbab Albite Granite Mining Area, Central Nubian Shield, Egypt. *Arab Journal of Nuclear Sciences and Applications*, 51 (4): 143-167.

Helba, H., Trumbull, R.B., Morteani, G., Khalil, S.O., and Arslan, A., 1997. Geochemical and petrographic studies of Ta mineralization in the Nuweibi albite granite complex, Eastern Desert, Egypt. *Mineralium Deposita*, 32(2): 164–179.

Helba, H.A., 1994. Geochemical prospecting for rare metals in Nuweibi area, central Eastern Desert, Egypt. PhD Thesis, Alexandria University, pp 145.

Holtz, F., Behrens, H., Dingwell, D.B., and Taylor, R.P., 1992. Water solubility in aluminosilicate melts of haplogranite composition at 2 kbar. *Chemical Geology*, 96: 289-302.

Irber, W., 1999. The lanthanide tetrad effect and its correlation with K/Rb, Eu/Eu*, Sr/Eu, Y/Ho, and Zr/Hf of evolving peraluminous granite suites. *Geochimica et Cosmochimica Acta*, 63: 89–508.

Irber, W., Möller, P., and Dulski, P., 1994. Two types of lanthanide tetrad effects observed in felsic igneous rocks. *European Journal of Mineralogy*, 1: 122.

Jahn, B.-M., Wu, F.Y., Capdevila, R., Martineau, F., Zhao, Z., and Wang, Y., 2001. Highly evolved juvenile granites with tetrad REE patterns: the Woduhe and Baerzhe granite from the Great Xing'an Mountains in NE China. *Lithos*, 59: 171-198.

Jahn, S., 1996. Geochemische und mineralogische Untersuchungen zur Metallogenese Seltenmetall-führender Granitoide in der Central Eastern Desert, Ägypten. Unpubl. Ph.D thesis, Technische Universität Berlin, 271 pp.

Jarrar, G.H., Manton, W.I., Stern, R.J., and Zachmann F., 2008. Late Neoproterozoic A-type granites in the northernmost Arabian-Nubian Shield formed by fractionation of basaltic melts. *Chemie der Erde*, 68: 295-312.

Johnson, P.R., 2003. Post-amalgamation basins of the NE Arabian shield and implications for Neoproterozoic III tectonism in the northern East African orogen. *Precambrian Research*, 123: 321-338.

Johnson, P.R., Halverson, G.P., Kusky, T.M., Stern, R.J., and Pease, V. 2013. Volcanosedimentary Basins in the Arabian-Nubian Shield: Markers of Repeated Exhumation and Denudation in a Neoproterozoic Accretionary Orogen. *Geosciences*, 3: 389-445.

Johnson, P.R., and Woldehaimanot, B., 2003. Development of the Arabian Nubian Shield: Perspectives on accretion and deformation in the East African Orogen and the assembly of Gondwana. In: M. Yoshida, B.F. Windley and S.

Dasgupta (Editors), Proterozoic East Gondwana: Supercontinent Assembly and Breakup. *Geological Society, London, Special Publication, London, pp*. 289-325.

Kamel, O.A., and E1Tabbal, H.K., 1980. Petrology and mineralogy of Nuweibi and Abu Dabbab rare metal apogranites, Eastern Desert, Egypt. *Proc. Geodynamic Evolution of the Afro-Arabic Rift System, Atti. Cony. Lincei*., 47: 685-705, Roma.

Katzir, Y., Eyal, M., Litvinovsky, B.A., Jahn, B.M., Zanilevich, A.N., Valley, J.W., Beeri, Y., and Shimshilashvili, E., 2007. Petrogenesis of A-type granites and origin of vertical zoning in the Katharina pluton, Gebel Mussa (Mt. Moses) area, Sinai, Egypt. *Lithos*, 95: 208-228.

Kessel, R., Stein, M., and Navon, O., 1998. Petrogenesis of late Neoproterozoic dikes in the northern Arabian-Nubian Shield: Implications for the Origin of A-type granites. *Precambrian Research*, 92: 195-213.

Khalil, A.E.S., Obeid, M.A. and Azer, M.K., 2014. Serpentinized peridotites at the north part of Wadi Allaqi district (Egypt): Implications for the tectono-magmatic evolution of fore-arc crust. *Acta Geologica Sinica - English Edition*, 88 (5): 1421-1436.

Khalil, A.E.S., Obeid, M.A., Azer, M.K., and Asimow, P.D., 2018. Geochemistry and petrogenesis of post-collisional alkaline and peralkaline granites of the Arabian-Nubian Shield: a case study from the southern tip of Sinai Peninsula, Egypt. *International Geology Review*, 60(8): 998-1018.

King, P.L., White, A.J.R., Chappell, B.W., and Allen, C.M., 1997. Characterization and origin of aluminous A-type granites from the Lachlan Fold Belt, southeastern Australia. *Journal of Petrology*, 38: 371-391.

Kovalenko, V.I., and Kovalenko, N.I., 1984. Problems of the origin, ore bearing and evolution of rare-metal granites. *Physics of the Earth and Planetary Interiors*, 35: 51-62.

Küster, D., 2009. Granitoid-hosted Ta mineralization in the Arabian- Nubian Shield: ore deposit types, tectono-metallogenetic setting and petrogenetic framework. *Ore Geology Review*, 35: 68–86.

Lee, S.-G., Asahara, Y., Tanaka, T., Lee, S.R., and Lee, T., 2013. Geochemical significance of the Rb–Sr, La–Ce and Sm–Nd isotope systems in A-type rocks with REE tetrad patterns and negative Eu and Ce anomalies: The Cretaceous Muamsa and Weolaksan granites, South Korea. *Chemie der Erde –Geochemistry*, 73: 75-88.

Liégeois, J.P., and Black, R., 1987. Alkaline magmatism subsequent to collision in the Pan-African belt of the Adrar des Iforas. In: Fitton, J.G., Upton, B.G.J. (Eds.), Alkaline Igneous Rocks. *Geological Society, Special Publication*, 30: 381-401.

Liégeois, J.P., Navez, J., Black, R., and Hertogen, J., 1998. Contrasting origin of post-collision high-K calc-alkaline and shoshonitic versus alkaline and peralkaline granitoids. The use of sliding normalization. *Lithos*, 45: 1-28.

London, D., 1987. Internal differentiation of rare element pegmatites: effects of boron, phosphorus, and fluorine. *Geochimica et Cosmochimica Acta*, 51: 403–420.

London, D., Morgan, G.B., Paul, K.A., and Guttery, B.M., 2012. Internal evolution of miarolitic granitic pegmatites at the Little Three Mine, Ramona, California, USA. *Canadian Mineralogist*, 50: 1025–1054.

Lundstrom, C.C., 2016. The role of thermal migration and low-temperature melt in granitoid formation: can granite form without rhyolitic melt? *International Geology Review*, 58(3): 371-388.

Manning, D.A.C., 1981. The effect of fluorine on liquidus phase relationships in the system Qz–Ab–Or with excess water at 1 kb. *Contribution to Mineralogy and Petrology*, 76: 206–215.

McKay, G.A., 1989. Partitioning of rare earth elements between major silicate minerals and basaltic melts. In: Lipin, B. R. & McKay, G. A. (eds.), Geochemistry and mineralogy of rare earth elements. *Mineralogical Society of America*, 21: 45-77.

Mechie, J., and Prodehl, C., 1988. Crustal and uppermost mantle structure beneath the Afro-Arabian rift system. *Tectonophysics*, 153: 103-121.

Meert, J.G., 2003. A synopsis of events related to the assembly of eastern Gondwana. *Tectonophysics*, 362: 1-40.

Miller, C.F., Stoddard, E.F., Bradfish, L.J., and Dollase, W.A., 1981. Composition of plutonic muscovite: genetic implications. *Canadian Mineralogist*, 19(1): 25-34.

Mittlefehldt, D.W., and Miller, C.F., 1983. Geochemistry of the Sweetwater Wash pluton, California: implications for ``anomalous'' trace element behaviour during differentiation of felsic magmas. *Geochimica et Cosmochimica Acta*, 47: 109-124.

Moghazi, A.K.M., Iaccheri, L.M., Bakhsh, R.A., Kotov, A.B., and Ali, K.A., 2015. Sources of rare-metal-bearing A-type granites from Jabel Sayed complex, Northern Arabian Shield, Saudi Arabia. *Journal of Asian Earth Sciences*, 107: 244–258.

Mohamed, A.M., 2013. Immiscibility between silicate magma and aqueous fluids in Egyptian raremetal granites: melt and fluid inclusions study. *Arabian Journal of Geosciences*, 6(10): 15-25.

Mohamed, F.H., 1993. Rare-metal-bearing and barren granites, Eastern Desert of Egypt: geochemical characterization and metallogenetic aspects. *Journal of African Earth Sciences*, 17: 525– 539.

Möller, P., and Muecke, G.K., 1984. Significance of Europium anomalies in silicate melts and crystal-melt equilibria: a re-evaluation. *Contribution to Mineralogy and Petrology*, 87: 242–250.

Morag, N., Avigad, D., Gerdes, A., Belousova, E., and Harlavan, Y., 2011. Crustal evolution and recycling in the northern Arabian-Nubian Shield: New perspectives from zircon Lu–Hf and U–Pb systematics. *Precambrian Research*, 186: 101-116.

Mushkin, A., Navon, O., Halicz, L., Heimann, A., Woerner, G., and Stein, M., 1999. Geology and geochronology of the Amram Massif, southern Negev Desert, Israel. *Israel Journal of Earth Sciences*, 48: 179–193.

Mushkin, A., Navon, O., Halicz, L., Hartmann, G., and Stein, M., 2003. The petrogenesis of A-type magmas from the Amram Massif, southern Israel. *Journal of Petrology*, 44(5): 815-832.

Müller, A., and Seltmann, R., 1999. The genetic significance of snowball quartz in high fractionated tin granites of the Krušne Hory/Erzgebirge Mineral deposits *processes to processing*, 1: 409-412.

Olade, M.A., 1980. Geochemical characteristics of tin bearing and tin-barren granites, northern Nigeria. *Economic Geology*, 75: 71-82.

Patiño Douce, A.E., 1999. What do experiments tell us about the relative contributions of crust and mantle to the origin of granitic magmas? In: Castro, A., Fernandez, C. & Vigneresse, J. (eds) Understanding Granites: Integrating New and Classical Techniques. *Geological Society, London, Special Publications*, 168: 55–75.

Pearce, J.A., 1983. Role of the sub-continental lithosphere in magma genesis at active continental margins. In: Hawkesworth, C.J., Norry, M.J. (Eds.), Continental Basalts and Mantle Xenoliths. Shiva, Nantwich, pp. 230-249.

Pichavant, M., and Manning, D., 1984. Petrogenesis of tourmaline granites and topaz granites; the contribution of experimental data. *Physics of the Earth and Planetary Interiors*, 35: 31–50.

Pollard, P.J., 1989. Geologic characteristics and genetic problems associated with the development of granite-hosted deposits of tantalum and niobium. In: Möller P, Cerny P, Saupe F (eds), Lanthanides, tantalum and niobium, Springer New York Berlin Heidelberg, pp 240-256.

Qadhi, T.M., 2007. Geochemical evolution of rare metal-bearing A-type granites from the Aja batholith, Hail Terrain, Saudi Arabia. *Journal of Geological Society of India*, *70*(5): 714.

Ramsay, C.R., 1986. Specialized felsic plutonic rocks of the Arabian Shield and their precursors. *Journal of African Earth Sciences*, 4: 153-168.

Renno, A., 1997. Zur Petrogenese der Albitgranite von Abu Dabbab und Nuweibi, Central Eastern Desert, Ägypten. Unpubl PhD thesis, Technische Universität Berlin, 216 pp.

Renno, A.D., Schmidt, W., and Shalaby, I.M., 1993. Rare-metal province cental Eastern Desert, Egypt. II A-Type granites of Abu Dabbab, Igla and Nuweibi. In: Thorweih, U., Schandelmeier, H. Eds.), geosciencentific research in NE Africa. Balkema, Rotterdam, Brookfield, 483-488.

Riad, A.M., 1979. Geology and petrology on some apogranite occurrence, Nuweibi area, Eastern Desert, Egypt. M Sc Thesis, Al-Azhar University, Cairo, Egypt.

Richard, L.R., 1995. Mineralogical and petrological data processing system. Minpet Software (c) 1988-1995, Version 2.02.

Rugless, C.S., and Pirajno, F., 1996. Geology and geochemistry of the Copperhead albitite ‘‘carbonate’’ complex, east Kimberley, Western Australia. *Australian Journal of Earth Sciences*, 43: 311-322.

Sabet, A.H., Tsogoev, V.B., Sarin, L.P., and Azazi, S.A., 1976. Tin–tantalum deposit of Abu Dabbab. *Annals of Geological Survey of Egypt*, VI: 93–118.

Samuel, M.D., Moussa, H.E., Azer, M.K., and Ghabrial, D.S., 2019. Geochemical constraints of the Ediacaran volcano-sedimentary succession at Wadi Zaghra, Sa'al Metamorphic Complex, South Sinai, Egypt. *Acta Geologica Sinica*, 93(1): 50–73.

Schwartz, M.O., 1992. Geochemical criteria for distinguishing magmatic and metasomatic albite-enrichment in granitoids: examples from the Ta–Li granite Yichun (China) and the Sn–W deposit Tikus (Indonesia). *Mineralium Deposita*, 27: 101-108.

Sherif, M.I., Ghoneim, M.F., Heikal, M.T.S., and El Dosuky, B.T., 2013. Perogenesis of granites, Sharm El-Sheikh area, South Sinai, Egypt: petrological constrains and tectonic evolution. *Mineralogy and Petrology*, 107: 765-783.

Sklyarov, E.V., Gladkochub, D.P., Kotov, A.B., Starikova, A.E., Sharygin, V.V., Velikoslavinsky, S.D., Larin, A.M., Mazukabzov, A.M., Tolmacheva, E.V., and Khromova, E.A., 2016. Genesis of the Katugin rare-metal ore deposit: Magmatism versus metasomatism. *Russian Journal of Pacific Geology*, 10(3): 155-167.

Srivastava, P.K., Gupta, Y.P., and Qazi, M.A., 2007. Geochemistry of Rare Metal Bearing A-Type Dhanota Granite, Mahendragarh District, Haryana. Journal *of Geological Society of India*, 70(2): 265.

Stern, R.J., 1985. The Najd Fault System, Saudi Arabia and Egypt: a late Precambrian rift-related transform system. *Tectonics,* 4: 497–511.

Stern, R.J., 1994. Arc assembly and continental collision in the Neoproterozoic East African Orogen: implications for the consolidation of Gondwanaland. *Annual Reviews of Earth and Planetary Science,* 22: 319-351.

Stern R.J., and Gottfried, D., 1986. Petrogenesis of a Late Precambrian (575-600 Ma) bimodal suite in Northeast Africa. *Contribution to Mineralogy and Petrology*, 92: 492-501.

Stern, R.J., and edge, C.E., 1985. Geochronologic constraints on late Precambrian crustal evolution in the Eastern Desert of Egypt. *American Journal of Science*, 285: 97–127.

Stern, R.J., and Voegeli, D.A., 1987. Geochemistry, geochronology, and petrogenesis of a late Precambrian (~590 Ma) composite dike from the North Eastern Desert of Egypt. *Geological Rundschau*, 76: 325-341.

Stoeser, D.B., and Frost, C.D., 2006. Nd, Pb, Sr, and O isotopic characterization of Saudi Arabian Shield terranes. *Chemical Geology*, 226: 163-188.

Sylvester, P.J., 1989. Post-collisional alkaline granites. Journal of Geology, 97: 261-280.

Tao, J., Li, W., Cai, Y., and Cen, T., 2014. Mineralogical feature and geological significance of muscovites from the Longyuanba Indosinian and Yanshannian two-mica granites in the eastern Nanling Range. *Science China Earth Sciences*, 57: 1150–1157.

Tischendorf, G., 1977. Geochemical and petrographic characteristics of silicic magmatic rocks associated with rare-metal mineralization. In: Stemprok, M., Burnol,, L. and Tischendorf, G. (eds.) Metalization Associated with Acid Magmatism 2, Usterdni Ustav Geologicky, Prague, 41-98.

Tkachev, A.V., 2011. Evolution of metallogeny of granitic pegmatites associated with orogens throughout geological time. *Geological Society of London, Special Publications*, 350(1): 7-23.

Tollo, R.P., Aleinikoff, J.N., Bartholomew, M.J., and Rankin, D.W., 2004. Neoproterozoic A-type granitoids of the central and southern Appalachians: intraplate magmatism associated with episodic rifting of the Rodinian supercontinent. *Precambrian Research,* 128: 3-38.

Vance, J.A., 1969. On Synneusis. Contributions to Mineralogy and Petrology, 24: 7-29.

Webb, P.C., Tindle, A.G., Barritt, S.D., Brown, G.C., and Miller, J.F., 1985. Radiothermal granites of the United Kingdom: comparison of fractionation patterns and variation of heat production for selected granites. *Inst. Min. Metal. Spec. Publ.,* pp.409-424.

Whalen, J.B., Currie, K.L., and Chappell, B.W., 1987. A-type granites: geochemical characteristics, discrimination and petrogenesis. *Contribution to Mineralogy and Petrology*, 95: 407-419.

Winkler, H.G.F., Boese, M., and Marcopoulos, T., 1975. Low temperature granite melts. *Neues Jahrbuch für Mineralogie. Monatshefte*, 6: 245–268.

Wu, F.-Y., Sun, D.-y., Li, H., Jahn, B.-m., and Wilde, S., 2002. A-type granites in northeastern China: age and geochemical constraints on their petrogenesis. *Chemical Geology*, 187: 143–173.

Yang, G., Li, Y., Wu, H., Zhong, X., Yang, B., Yan, C., Yan, J., and Si, G. 2011. Geochronological and geochemical constrains on petrogenesis of the Huangyangshan A-type granite from the East Junggar, Xinjiang, NW China. *Journal of Asian Earth Sciences*, 40: 722-736.

Zhao, Z.H., Xiong, X.L., Han, X.D., Wang, Y.X., Wang, Q., Bao, Z.W., and Jahn, B.M., 2002. Controls on the REE tetrad effect in granites: evidence from the Qianlishan and Baerzhe granites, China. *Geochemical Journal*, 36: 527–543.

Zhu, Y.F., Zeng, Y., and Gu, L., 2006. Geochemistry of the rare metal-bearing pegmatite No. 3 vein and related granites in the Keketuohai region, Altay Mountains, northwest China. *Journal of Asian Earth Sciences*, 27(1): 61-77.

Zhu, Z., Wang, R., Marignac, C., Cuney, M., Mercadier, J., Che, X., and Lespinasse, M.Y., 2018. A new style of rare metal granite with Nb-rich mica: The Early Cretaceous Huangshan rare-metal granite suite, northeast Jiangxi Province, southeast China. *American Mineralogist*, 103(10): 1530-1544.

Figure Captions

About the first author

Bassam A. ABU-AMARAH, born in 1959 in Al Madina, Al Mounawarah, Saudi Arabia; B.Sc 1981 from King Saud Universitry; M.Phil. and Ph.D. 1990 from Manchester University, UK. Professor of geological sciences, specializing in the fields of mineralogy, petrology and geochemistry, with particulate interest the mineralogy, economic ore deposits, petrogenesis and geochemistry of the Arabian Shield. E-mail: babuamarah@ksu.edu.sa.